Journal of Biomedical Optics

BiomedicalOptics.SPIEDigitalLibrary.org

In vivo imaging of human oral hard and soft tissues by polarization-sensitive optical coherence tomography

Julia Walther
Jonas Golde
Lars Kirsten
Florian Tetschke
Franz Hempel
Tobias Rosenauer
Christian Hannig
Edmund Koch

SPIE.

Julia Walther, Jonas Golde, Lars Kirsten, Florian Tetschke, Franz Hempel, Tobias Rosenauer, Christian Hannig, Edmund Koch, "*In vivo* imaging of human oral hard and soft tissues by polarization-sensitive optical coherence tomography," *J. Biomed. Opt.* **22**(12), 121717 (2017), doi: 10.1117/1.JBO.22.12.121717.

In vivo imaging of human oral hard and soft tissues by polarization-sensitive optical coherence tomography

Julia Walther,[a,b,*,†] Jonas Golde,[a,†] Lars Kirsten,[a] Florian Tetschke,[a,c] Franz Hempel,[a] Tobias Rosenauer,[c] Christian Hannig,[c] and Edmund Koch[a]
[a]TU Dresden, Faculty of Medicine Carl Gustav Carus, Anesthesiology and Intensive Care Medicine, Clinical Sensoring and Monitoring, Dresden, Germany
[b]TU Dresden, Faculty of Medicine Carl Gustav Carus, Department of Medical Physics and Biomedical Engineering, Dresden, Germany
[c]TU Dresden, Faculty of Medicine Carl Gustav Carus, Policlinic of Operative and Pediatric Dentistry, Dresden, Germany

Abstract. Since optical coherence tomography (OCT) provides three-dimensional high-resolution images of biological tissue, the benefit of polarization contrast in the field of dentistry is highlighted in this study. Polarization-sensitive OCT (PS OCT) with phase-sensitive recording is used for imaging dental and mucosal tissues in the human oral cavity *in vivo*. An enhanced polarization contrast of oral structures is reached by analyzing the signals of the co- and crosspolarized channels of the swept source PS OCT system quantitatively with respect to reflectivity, retardation, optic axis orientation, and depolarization. The calculation of these polarization parameters enables a high tissue-specific contrast imaging for the detailed physical interpretation of human oral hard and soft tissues. For the proof-of-principle, imaging of composite restorations and mineralization defects at premolars as well as gingival, lingual, and labial oral mucosa was performed *in vivo* within the anterior oral cavity. The achieved contrast-enhanced results of the investigated human oral tissues by means of polarization-sensitive imaging are evaluated by the comparison with conventional intensity-based OCT. [DOI: 10.1117/1.JBO.22.12.121717]

Keywords: optical coherence tomography; dentistry; polarization contrast; medical and biological imaging; tissue.

Paper 170509SSR received Aug. 3, 2017; accepted for publication Nov. 27, 2017; published online Dec. 20, 2017.

1 Introduction

Various biological tissues change the polarization of light, for which reason tissue polarization properties can be important for the diagnosis of pathological alterations in tendons, bones, cartilages, teeth, and skin. Biological media are often birefringent caused by asymmetrically oriented structures, e.g., collagen fibers and dentinal microtubules, as well as molecular and mineralized compositions in biological tissue. Since polarization imaging is innovative and promising for medical diagnosis of pathologies, technical solutions for clinical *in vivo* applications are in demand. Because optical coherence tomography (OCT) is a prospective noninvasive imaging technique for three-dimensional high-resolution imaging of subsurface tissue morphology[1–4] with the possibility of functional imaging by polarization-sensitive OCT (PS OCT), it is attractive for depth-resolved tissue-specific contrast imaging with high speed and sensitivity *in vivo*. Although conventional intensity-based OCT provides a high spatial resolution in the micrometer range, tissue micro- and nanostructures cannot be resolved optically. By detecting the polarization change of the reflected light with PS OCT, properties of polarization changing microstructures can provide information of early pathological alterations before morphological tissue remodeling occurs in larger scale detectable with intensity-based OCT.[5,6]

Early and also some recent work of PS OCT is based on PS low coherence reflectometry, demonstrated first by Hee et al.,[7] and the measurement of the phase retardation between orthogonal linear polarization modes in birefringent samples.[8] Today, this method is referred to as PS OCT with single circular input state, which provides quantitative polarization contrast for all possible optic axis orientations of the sample.[9] Beyond the technical advancements in terms of light sources and fast detection units, PS OCT was evolved by different detection schemes with multiple input states as well as improved data processing. Initially,[7,8] the reflectivity and retardation of a sample were measured for the determination of birefringence as a function of the depth. By the enhancement of phase-sensitive detection of the interferometric signals in two orthogonal polarization channels, a third important parameter for physical interpretation of a birefringent sample, the orientation of the fast optical axis of the sample, can be determined.[10–12] An additional relevant parameter, the degree of polarization uniformity (DOPU), is based on averaged Stokes vector elements and proposed for imaging and segmentation of local variations of the polarization state[13,14] also known as depolarization or rather polarization scrambling as an intrinsic tissue property.[15]

Equipped with these advancements, PS OCT is increasingly applied for medical diagnosis mainly in ophthalmology[9,16–18] followed by dentistry,[19,20] cardiology,[6,21,22] and dermatology[23–25] with regard to the frequency of publications over the last years.[9] Although PS OCT has successfully shown to provide additional contrast for distinguishing pathological lesions from normal tissues, it has not been used much in the oral cavity. While the measurement of the birefringent behavior of hard dental tissues by PS OCT is already addressed in biomedical research,[26–28] the polarization properties of oral soft tissue *ex vivo* and *in vivo* are investigated only by a few studies,[29–32] although the presented

*Address all correspondence to Julia Walther, E-mail: julia.walther@tu-dresden.de

†Equal contribution.

results show that it is worthwhile for quantitative imaging. Regarding dental PS OCT, most of the research is performed using linear incident light,[19,20,33–39] in consequence of which the fast or slow birefringent axis could align with the linear polarization such that no or reduced birefringence is measured.[40] Although, first work of PS OCT in dentistry has used circular polarized light incidence[26,41] and considered the phase retardation[27,42] for imaging the birefringence in tooth structures, the argument for a single linear input state is the suppression of the Fresnel surface reflection in the crosspolarization channel.[35,36,43]

Based on the simplicity of a single circular input state (requiring only one simultaneous measurement of both orthogonally polarized light spectra per sample location) and the amount of information for physical interpretation of tissues by phase-sensitive PS OCT, we propose to image birefringent oral hard and soft tissues with circularly polarized light[44] in combination with the analysis of reflectivity, retardation, optic axis orientation,[12] and depolarization[13,14] as advanced calculation of polarization contrast in PS OCT today. We show that surface reflections and birefringent behavior in dental hard tissues present no difficulty and—quite the opposite—are advantageous for the detection of early alterations. To the best of our knowledge, the algorithms for optic axis orientation and DOPU[13,14,16] in combination with reflectivity and retardation are first used for the *in vivo* imaging of oral tissue structures with the outcome of an enhanced tissue structure contrast in comparison to conventional intensity-based OCT.

2 Materials and Methods

2.1 *Experimental Setup*

For the pilot study, we are using an OCT system that provides depth-resolved polarization contrast of samples utilizing an established layout that was initially proposed by Hee et al.[7] and most recently implemented in fiber-based swept source systems.[25] Our setup is based on a modification of a self-built swept source OCT system, which is adapted for polarization-sensitive measurement by a new scanner head with bulk optics and corresponding fiber optics. The schematic of the resulting PS OCT system is shown in Fig. 1. As shown, the light of the swept laser (Axsun 1310 Swept Source Engine, Axsun Technologies Inc.) with a center wavelength of $\lambda_0 = 1310$ nm and a used bandwidth of $\Delta\lambda = 110$ nm is sent to a fiber Bragg grating (FBG) that is applied for A-scan triggering. After a further amplification by a booster optical amplifier (BOA), the light is sent via an optical circulator (OC) to the scanner head with free space optics. There, the light is split into vertical and horizontal linearly polarized lights by a polarization beam splitter (PBS). Only the vertically polarized light is transmitted to the interferometer and split into the reference and sample arms with equal intensities by a polarization-insensitive beam splitter (BS). In the sample arm, the linearly polarized light is transformed into circularly polarized light by a quarter-wave plate (QWP1) with the fast axis orientated at 45 deg relative to the vertical direction. The backscattered light from within the sample passes again QWP1 resulting in an arbitrary elliptical polarization of the sample light in dependence on the birefringence properties of the sample. Without birefringence in the sample, e.g., reflection on a mirror, the light that double passed the QWP1 will be horizontally polarized. In the reference arm, the quarter-wave plate (QWP2) is set to 22.5 deg with respect to the vertical axis to generate a linearly polarized reference beam at 45 deg relative to the incoming beam due to double passing QWP2. After recombining the light of both arms at BS, the interference light is separated into vertically (y-axis) and horizontally (x-axis) polarized signals by a PBS. Since the extinction ratio of the horizontally and vertically polarized lights for the reflected beam amounts only to 100 : 1, two additional linear polarizers (LPo) are used in the copolarization channel to suppress the vertically polarized light. The simultaneous detection of both orthogonally polarized interference signals $I_x(k)$ (copolarized channel) and $I_y(k)$ (crosspolarized channel) is realized by dual-balanced detection to reject common-mode noise and improve the signal-to-noise ratio of the system. To acquire inference signals that are linear in k-space, the clock signal of

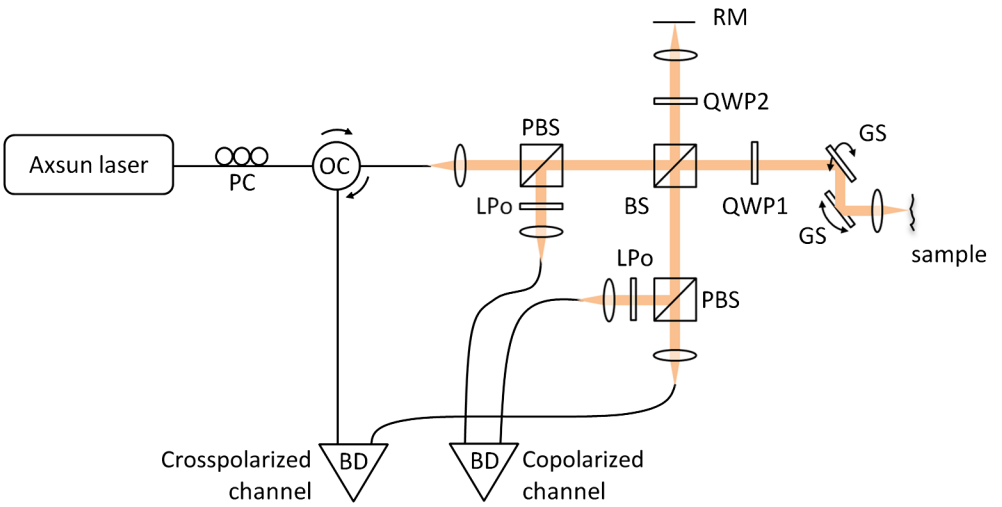

Fig. 1 Swept source OCT system with polarization-sensitive scanner head. Swept laser with $\lambda_0 = 1310$ nm and $\Delta\lambda = 110$ nm. FBG, fiber Bragg grating; PC, polarization controller; BOA, booster optical amplifier; OC, optical circulator; PBS, polarization beam splitter; LPo, linear polarizer; BS, polarizaton-independent beam splitter; QWP1, quarter-wave plate oriented at 45 deg; QWP2, quarter-wave plate oriented at 22.5 deg; RM, reference mirror; GS, galvanometer scanners; BD, balanced detectors; DA, data acquisition card.

the swept laser is utilized as a sampling trigger of the high-speed digitizer (ATS9360, Alazar Technologies Inc.). The backscattered light of nonbirefringent structures will be detected in the horizontal polarization channel, which is referred to as copolarization channel.[45] In dependency on the amount of birefringence of the sample, a corresponding fraction of light backscattered in and behind birefringent structures will be detected in the crosspolarization channel.

For oral imaging, a set of 1280×1280 A-scans was acquired over an area 10×10 mm at an A-scan rate of 50 kHz resulting in a B-scan rate of ~40 fps. The lateral resolution amounts to 15.6 μm. The axial resolution is measured to be 15.1 μm. Data acquisition and image processing are completely controlled using customized LabVIEW™ (National Instruments Inc.) and Fiji[46] software.

2.2 *Determination of the Polarization Contrast*

Since the basics of PS OCT analysis, regarding the principles of light polarization and polarization effects as well as polarization properties of tissue described by the Jones and Stokes formalism, have been summarized most recently in detail by de Boer et al. and Baumann et al.,[9,16] the calculation of the polarization contrast of tissue is described briefly in this section. As shown in Fig. 1, the interference signal of the copolarized $I_x(k)$ and the crosspolarized channel $I_y(k)$ are detected by balanced detection units as a function of the wavenumber k. As conventionally done for Fourier domain OCT, the depth-resolved scan (A-scan) is calculated from an inverse Fourier transform of the interference signal with the result of two complex A-scans for both orthogonal polarization states as

$$\begin{aligned} \mathrm{FT}^{-1}\{I_x(k)\} &\rightarrow \Gamma_x(z) = A_x(z)e^{i\varphi_x(z)} \\ \mathrm{FT}^{-1}\{I_y(k)\} &\rightarrow \Gamma_y(z) = A_y(z)e^{i\varphi_y(z)}, \end{aligned} \tag{1}$$

where the parameter z corresponds to the depth coordinate with respect to the position of the reference mirror (cp. RM in Fig. 1).[12] For polarization contrast imaging, sample reflectivity $R(z)$, retardation $\delta(z)$, and sample optic axis orientation $\theta(z)$ are calculated from the amplitudes $[A_{x/y}(z)]$ and phase information $[\varphi_{x/y}(z)]$.

$$\begin{aligned} R(z) &\propto A_x(z)^2 + A_y(z)^2 \\ \delta(z) &= \arctan\left[\frac{A_y(z)}{A_x(z)}\right] \\ \theta_s(z) &= \frac{\pi - \Delta\varphi(z)}{2} \\ \Delta\varphi(z) &= \varphi_y(z) - \varphi_x(z). \end{aligned} \tag{2}$$

The unambiguous measurement ranges are $[0; \pi/2]$ for the retardation $\delta(z)$ and $[-\pi/2; \pi/2]$ for the fast birefringent axis orientation $\theta(z)$. By means of the detected amplitudes $[A_x(z), A_y(z)]$ and corresponding phase differences $\Delta\varphi$, the Stokes vector elements I, Q, U, and V calculated for each depth pixel can be determined by Eq. (3). This forms the basis for the calculation of the DOPU defined by Eq. (4),[13,14] where the normalized Stokes vector components are averaged within a sliding two-dimensional evaluation kernel for DOPU calculation. For the measurement results in Sec. 3, a kernel size of 6×6 is used for DOPU imaging.

$$S = \begin{pmatrix} I \\ Q \\ U \\ V \end{pmatrix} = \begin{pmatrix} A_x^2 + A_y^2 \\ A_x^2 - A_y^2 \\ 2A_xA_y \cos\Delta\varphi \\ 2A_xA_y \sin\Delta\varphi \end{pmatrix}, \tag{3}$$

$$\mathrm{DOPU} = \sqrt{Q_{\mathrm{norm,mean}}^2 + U_{\mathrm{norm,mean}}^2 + V_{\mathrm{norm,mean}}^2}. \tag{4}$$

Since a tissue layer can be simplified as a retarder plate of arbitrary thickness, retardation, and optic axis orientation, the theoretically expected PS OCT measurement values of $\delta(z)$ and $\theta(z)$ can be calculated for every possible retardation (in the range of $[0; 2\pi]$) and optic axis orientation (in the interval of $[0; \pi]$) of the sample as shown in Figs. 2(a) and 2(b). For this purpose, we assumed perfect PBSs as well as quarter-wave plates and simulated polarization-sensitive interference measurements based on the beam paths shown in Fig. 1 and by utilizing the Jones calculus (in correspondence to de Boer et al.[16]). The arbitrary retardation and optic axis orientation are thereby theoretically embodied by a variable retarder with specific optic axis orientation (representative for a birefringent tissue layer) that is passed forward and backward by a sample beam reflected below. Finally, the determined amplitudes and phase information for both channels were converted into optical parameters, according to Eq. (2).

For a defined fast axis orientation of the homogeneously birefringent sample, the measured cumulative retardation $\delta(z)$ and optic axis orientation $\theta(z)$ can be read as a function of the retardation of the sample, corresponding to a vertical line in the simulation maps, which is helpful for the analysis of the polarization contrast images of birefringent biological tissue. As shown in Fig. 2(b), the measured retardation is unambiguous for values less than $\pi/2$ and the measured optic axis orientation shows a $\pi/2$-jump at multiples of $\pi/2$ of the retardation of

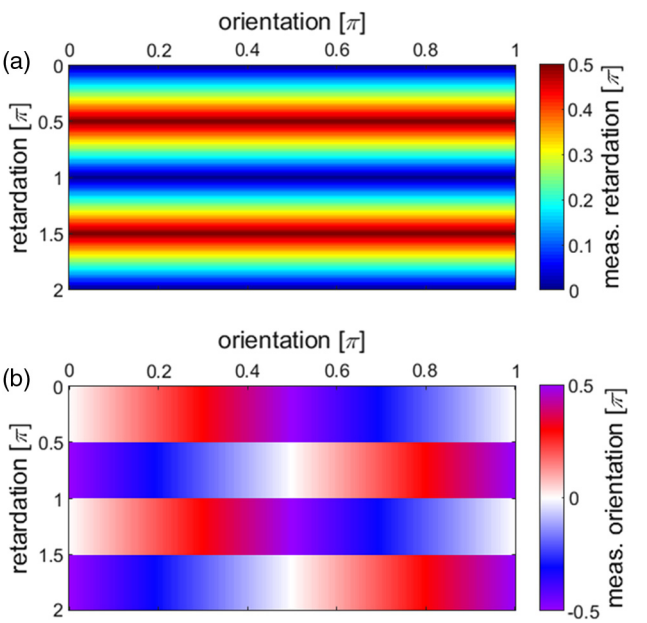

Fig. 2 (a) Simulation for the measurement of the cumulative phase retardation $\delta(z)$ and (b) optic axis orientation $\theta(z)$ of a linear retarder plate with variable phase retardation and optic axis orientation by PS OCT. By means of this map, polarization contrast images of birefringent samples by PS OCT can be easier interpreted.

the sample. To visualize the measured optic axis orientation for a constant retardation without any color jump, the transition from red to blue was adjusted with violet.

2.3 *Dental and Mucosal Background for PS OCT*

Since PS OCT will be used in this study for imaging the polarization properties of oral tissues, the polarization changing oral hard and soft structures are briefly described in this section. Starting with hard oral tissue, teeth can be considered as composites of enamel and dentin. Enamel as the hardest substance in the human body is highly mineralized. The inorganic content consists of dense packages of millions of elongated hydroxyapatite (HAP) crystals forming the enamel prisms.[47] The subsequent dentin equals a bonelike structure composed of different volume fractions of ceramics (HAP), protein (mostly collagen), and water. The mineralized collagen fibrils are an essential element of the regularly aligned micrometer-sized dentin tubules.[48] The boundary between the enamel and dentin is the so-called dentin–enamel junction (DEJ). Tooth structures relevant for PS OCT are primarily the HAP crystals in combination with the linear arrangement to enamel prisms causing birefringence.[26,27] Since the amount of HAP is smaller in the intertubular dentin, the birefringence effect in dentin is expected to be less developed than in enamel.

In soft oral tissue, linear ordered collagen fibers in the lamina propria are showing birefringence in contrast to the adjacent basement membrane, epithelium, and keratin layer[29] with no polarization changing content. Collagen fibrils are organized to fibril bundles, arranged in collagen fibers of different thicknesses, and embedded in the connective tissue of the reticular layer of the lamina propria. While the collagen fiber bundles of the lining oral mucosa are linearly aligned, the bundles in the dentogingival unit of the gingiva run in various directions. Regarding specialized oral mucosa, e.g., the dorsum of the tongue, collagen fibers can be found within the connective tissue core of each papilla and in the transition part between papillae as well as beneath in the laminar propria[49] and may cause birefringence.

For the pilot study, we have imaged representative dental and mucosal structures of the anterior oral cavity of two volunteers (A: male 30 years, B: female 33 years) *in vivo*. Prior to the PS OCT measurements, oral examination was performed by an experienced dentist in order to select specific regions accessible for *in vivo* dental imaging and to diagnose pathological alterations. Photographic overviews of the oral cavity were made for the allocation of the imaged regions (cp. Fig. 3). Besides the imaging of healthy lingual, labial, and gingival oral mucosa as well as inconspicuous tooth structures, a composite restoration at incisor 11 and a mineralization defect at premolar 24 of volunteer A as well as the cervical area of premolar 24 of volunteer B are imaged by PS OCT. All measurements were performed in contact mode by an attached distance piece in order to reduce motion artifacts.

3 Results

3.1 *PS OCT Imaging of Healthy Human Incisor In Vivo*

The imaging of the polarization contrast parameter retardation $\delta(z)$, optic axis orientation $\theta(z)$, and DOPU [cp. Eqs. (2)–(4)] will initially be explained on the example of the healthy

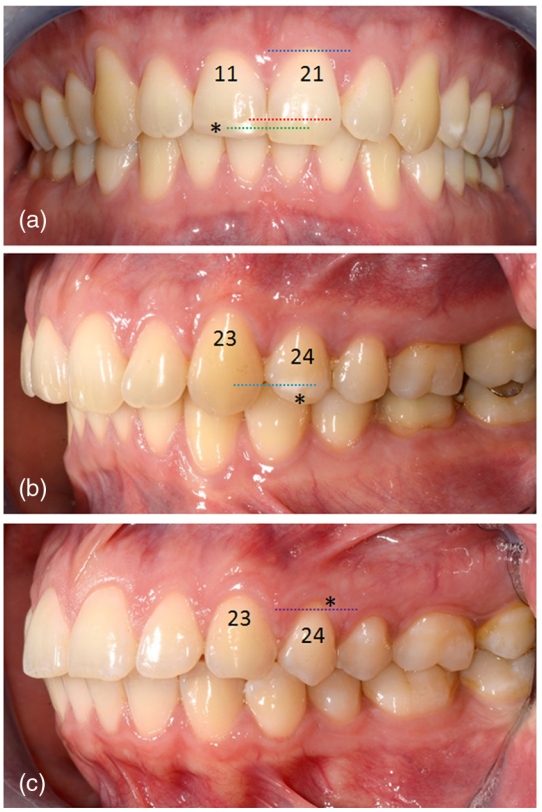

Fig. 3 Photographic overview of teeth and peridontium of (a, b) volunteers A and (c) B, respectively. Healthy mucosal and dental structures, the composite restoration at incisor 11 [asterisk in (a)] and the mineralization defect at premolar 24 [asterisk in (b)] of volunteer A as well as the cervical area of tooth 24 [asterisk in (c)] of volunteer B are imaged. The colored horizontal dashed lines indicate the position of the representative B-scans in Sec. 3. Red dashed line: Fig. 4, green dashed line: Fig. 5, bright blue dashed line: Fig. 6, violet dashed line: Fig. 7, and dark blue dashed line: Fig. 8.

permanent incisor 21 of volunteer A before considering dental alterations. The images acquired separately by the co- and cross-polarization channels as well as the calculated reflectivity image are shown in Figs. 4(a)–4(c). The copolarization channel [cp. Fig. 4(a)] contains the regular backscattering of nonpolarizing and nonbirefringent structures, whereas birefringent and polarization changing structures partly transfer light into the crosspolarization channel [cp. Fig. 4(b)]. The main backscattering signal of deeper structures is contained in the crosspolarization channel [cp. Fig. 4(b)] because of the polarization changing property of enamel and dentin. In this context, Chen et al. have concluded that the reason for the polarization behavior of dental structures imaged by PS OCT with circularly polarized light is caused by different polarization mechanics.[45] While birefringence is mainly reasonable for enamel, it is stated in Ref. 45 that multiple scattering rather than birefringence could be primarily causal for the transfer of light field energy from the co- to the crosspolarization channel for dentin (referred to as polarization memory effect in Ref. 45). Combining the backscattering signals to the common reflectivity information [cp. Fig. 4(c)], the sample structure can be shown free from birefringence artifacts such as periodic birefringence bands within the enamel. Clearly, a weak boundary within the enamel can be identified, which is probably assigned to different enamel types delimited by varying orientation of enamel prisms. Apparently,

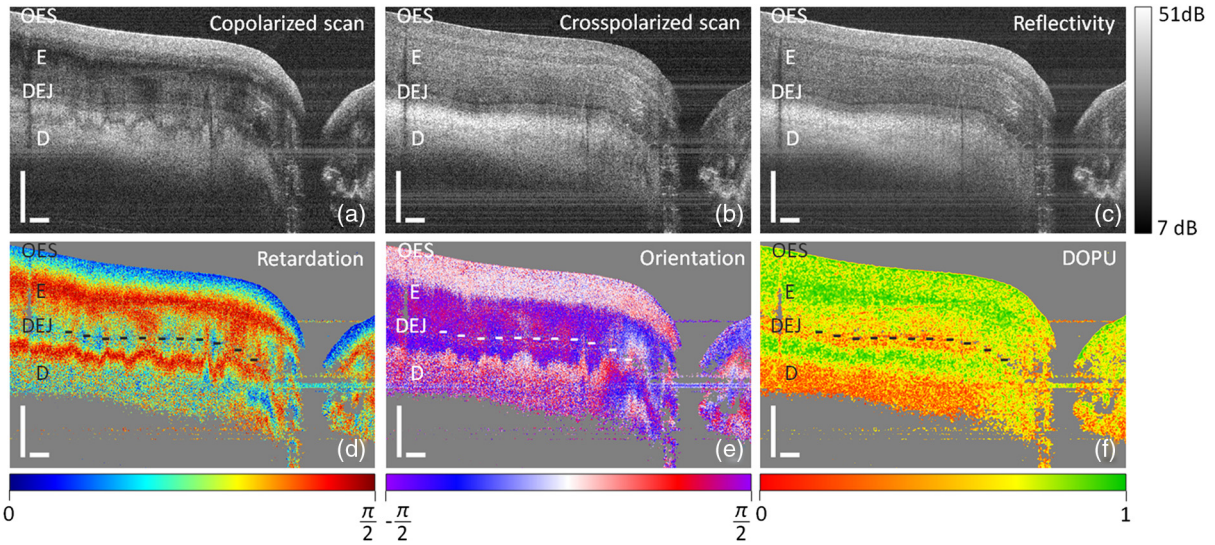

Fig. 4 Single OCT B-scans of (a) the copolarization and (b) crosspolarization channel as well as (c) the determined reflectivity image recorded of the OES, the enamel (E), DEJ, and dentin (D) of the healthy tooth 21 *in vivo*. The approximate location of the B-scans is related to the red dashed line in Fig. 3(a). For polarization contrast imaging, (d) the phase retardation, (e) the optic axis orientation, and (f) the DOPU is calculated. The black/white dashed line in (d–f) marks the DEJ on the basis of the reflectivity image in (c). Scale bars correspond to 500 μm. The scale bar in depth direction is adjusted on the refractive index of enamel in the 1300 nm range of 1.631.[51]

the reflectivity below the DEJ in dentin is initially low and increases at larger depth, which could correspond to the transition zone of mantle dentin and circumpulpal dentin differing in the amount, size, and configuration of collagen fibrils.[50] The horizontal stationary stripes appearing in different depths within the cross sectional images are probably caused by high-frequency signal components of the balanced detectors, which are mirrored into lower imaging frequencies and visible due to an imprecise background correction. Furthermore, the ratio between axial and lateral pixel sizes is not corrected for the optimal presentation of depth information and the axial depth is consistently adjusted on the refractive index of enamel in the 1300 nm wavelength range of 1.631.[51]

The image parts of Figs. 4(d)–4(f) present the PS OCT images of the retardation $\delta(z)$, optic axis orientation $\theta(z)$, and DOPU of the labial surface of the healthy incisor 21 with marked DEJ (black/white dashed line). A threshold value at a total reflectivity of 21 dB was chosen for eliminating background noise by a gray mask. Because the measurement of the retardation and optic axis orientation is cumulative over depth, the retardation is initially close to zero at the outer enamel surface (OES) and increases as a function of the light path in the birefringent enamel for which reason the retardation appears as a colored banded structure over depth [cp. Fig. 4(d)]. As the labial surface of tooth 21 was measured close to the incisal edge, the incident light beam is oblique or rather perpendicular to the longitudinal axis of the enamel prisms in the outer enamel region resulting in a strong birefringence effect as shown in Fig. 4(d). Toward the DEJ, $\delta(z)$ varies in the lateral direction and shows an increased noise, which could be caused by structural characteristics at this border, e.g., enamel tufts and spindles. Regarding the polarization effect below the DEJ, a strong retardation $\delta(z)$, visible as abrupt color change to red and back, could be measured apparently caused by a birefringent structure within the dentin. The noisy retardation below probably appears due to the combination of multiple scattering.[45]

Considering the optic axis orientation, two main regions within the enamel become apparent, around $\theta(z) = 0$ (upper region of E) and $\theta(z) = \pi/2$ (lower region of E). Since the measurement of the optic axis orientation is cumulative, a phase jump from zero (white color) to $\pi/2$ (violet color) appears for the measured $\theta(z)$ at a sample axis orientation of zero and a retardation of $\pi/2$ [cp. Fig. 2(b)], whereas the main orientation of the enamel prisms is retained. This effect is caused by the measurement method itself resulting in a cumulative measured axis orientation, sometimes referred to as artifact. Regarding the region below the DEJ, the measured $\theta(z)$ of the circumpulpal dentin is zero too, corresponding to a phase jump from $\theta(z) = \pi/2$ (violet color) to $\theta(z) = 0$ (white color) due to the cumulative measurement of $\theta(z)$. The calculated DOPU image in Fig. 4(f) confirms the interpretation of Figs. 4(d) and 4(e). Again, this is caused by the cumulatively measured retardation and axis orientation of OCT.

3.2 *PS OCT Imaging of Dental Alterations In Vivo*

Since PS OCT provides additional contrast for dental OCT imaging, conspicuous tooth structures within the anterior oral cavity are investigated. First, the labial surface of the central incisors of volunteer A was selected for imaging the differences in depth structure between tooth 11 with a composite restoration and the healthy tooth 21 [cp. Fig. 3(a)]. The reflectivity images calculated on the basis of Eq. (2) are presented for three representative B-scans of the detected volume scan in Figs. 5(a), 5(d), and 5(g). There, the composite restoration at tooth 11 characterized by a homogeneous backscattering signal can be clearly differentiated from the subjacent tooth structure. Interestingly, the underlying enamel structure contains a distinct crack [plus sign in Figs. 5(a), 5(d), and 5(g)], which is probably caused from dental trauma and continuously detected through the entire volume scan. Moreover, small cracks [green arrow in Fig. 5(d)] and interfacial gaps [green arrow in Fig. 5(g)] are visible at the edge

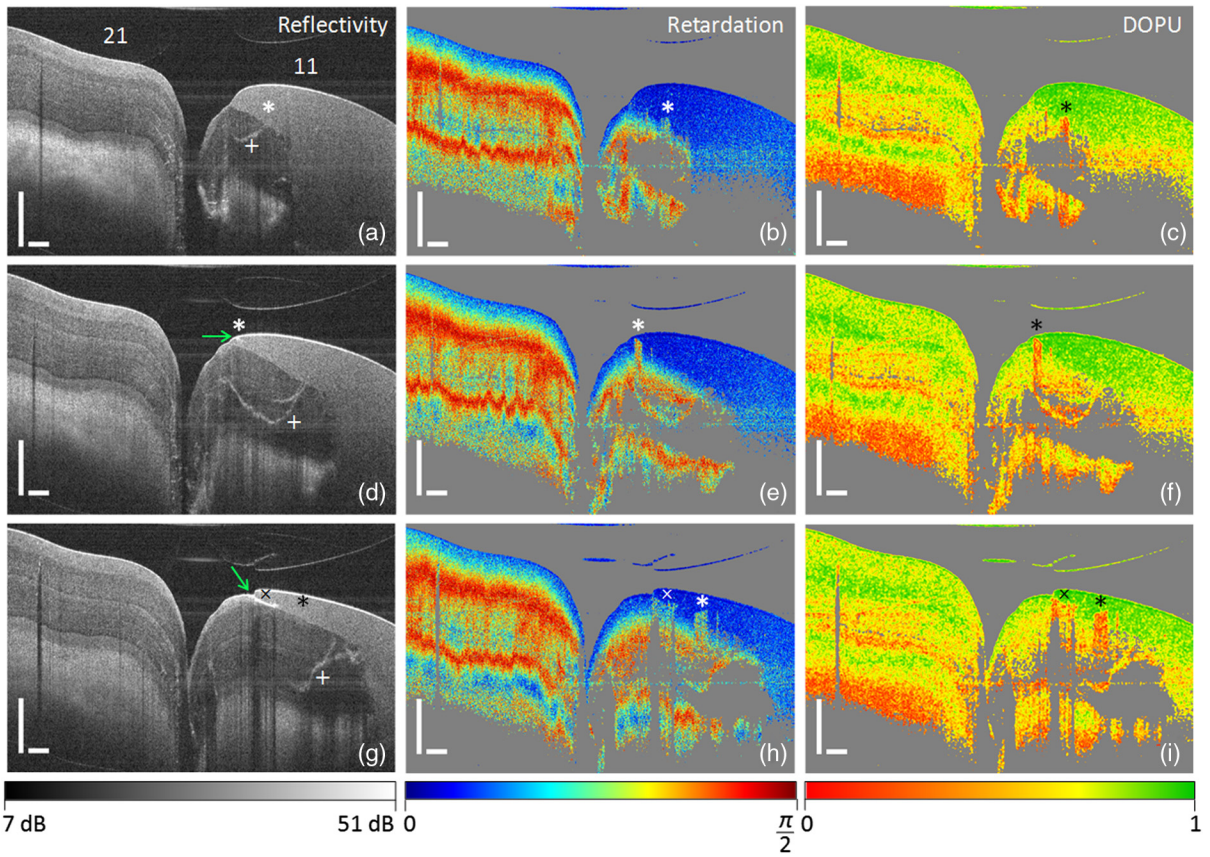

Fig. 5 Composite restoration at the proximal region of tooth 11 in comparison to the inconspicuous tooth 21 of volunteer A imaged by PS OCT. Image series showing (a, d, g) the reflectivity, (b, e, h) retardation, and (c, f, i) DOPU content of three representative B-scans of the detected volume scan. The approximate location of the B-scans is related to the green dashed line in Fig. 3(a). Plus sign: continous distinct crack within the enamel. Asterisk and cross sign: small regions of depolarization within and below the composite. Scale bars correspond to 500 μm. (Copolarized, crosspolarized, and optic axis orientation images in the appendix Figs. 13 and 14).

region of the restoration. Regarding polarization-sensitive imaging, the retardation, and DOPU images in Figs. 5(b), 5(e), 5(h) and 5(c), 5(f), 5(i) contain additional information of the composite restoration not detectable with classic intensity-based OCT [represented by Figs. 5(a), 5(d), and 5(g)]. Since the composite equals a random turbid media with spherical scatterers, the polarization of the incident light is retained in the backscattered portion for which reason no polarization contrast [$\delta(z) = 0$ in Figs. 5(b), 5(e), and 5(h)] is present. Consequently, the backscattered light is almost completely detected in the copolarization channel and only a negligible amount is noticeable in the crosspolarization channel probably due to multiple scattering. Apparently, small polarization changing regions [marked by the asterisks and cross sign in Figs. 5(b), 5(e), and 5(h)] exist within the composite visible by a rapid change of retardation in comparison to the surrounding region. There, the measured retardation shows a strongly increased noise representing a high degree of depolarization, which is confirmed by the DOPU images in Figs. 5(c), 5(f), and 5(i). Although the medical interpretation of this effect is not clear, the incident circularly polarized light is depolarized underneath the small crack [asterisk in Fig. 5(e)], the interfacial gap [cross sign in Fig. 5(h)], and within the composite itself [asterisks in Figs. 5(b) and 5(h)]. These regions probably contain inhomogeneously distributed birefringent substances (arising from the enamel, e.g., HAP and/or the composite) resulting in a measurable depolarization of the backscattered light. Since structures beneath are imaged with depolarized light, the polarization contrast gets lost for deeper birefringent tissues. Besides the visible dental structures, imaging artifacts appear due to a coherence revival in the swept laser and internal reflections of the optical setup, which is especially discoverable on the upper right-hand side of the images.

Second, a mineralization defect at the buccal side of tooth 24 of volunteer A is imaged [cp. Fig. 3(b)]. Three B-scans of the volume scan are selected as example for near-surface [Figs. 6(a)–6c)] and deep [Figs. 6(d)–6(f)] demineralization in comparison to inconspicuous neighboring areas [Figs. 6(g)–6(i)]. The near-surface mineralization defect shows a strong backscattering signal and a high depolarization underneath as shown in Figs. 6(a)–6(c). The signal below the mineralization defect is not corresponding to real tooth structure but rather caused by multiple scattered light having a longer light path for which reason an apparent backscattering signal with strong depolarization occurs in deeper regions. Interestingly, the deeper demineralization causes a less strong backscattering signal and a smaller amount of multiple scattering leading to a smaller DOPU as seen in Figs. 6(d)–6(f). Nevertheless, DOPU provides a strong contrast for distinct mineralization defects.

Third, the cervical area of the buccal side of the premolar 24 of volunteer B is measured. As shown in Figs. 7(a)–7(c), exposed dentin, which was diagnosed by the dentist before

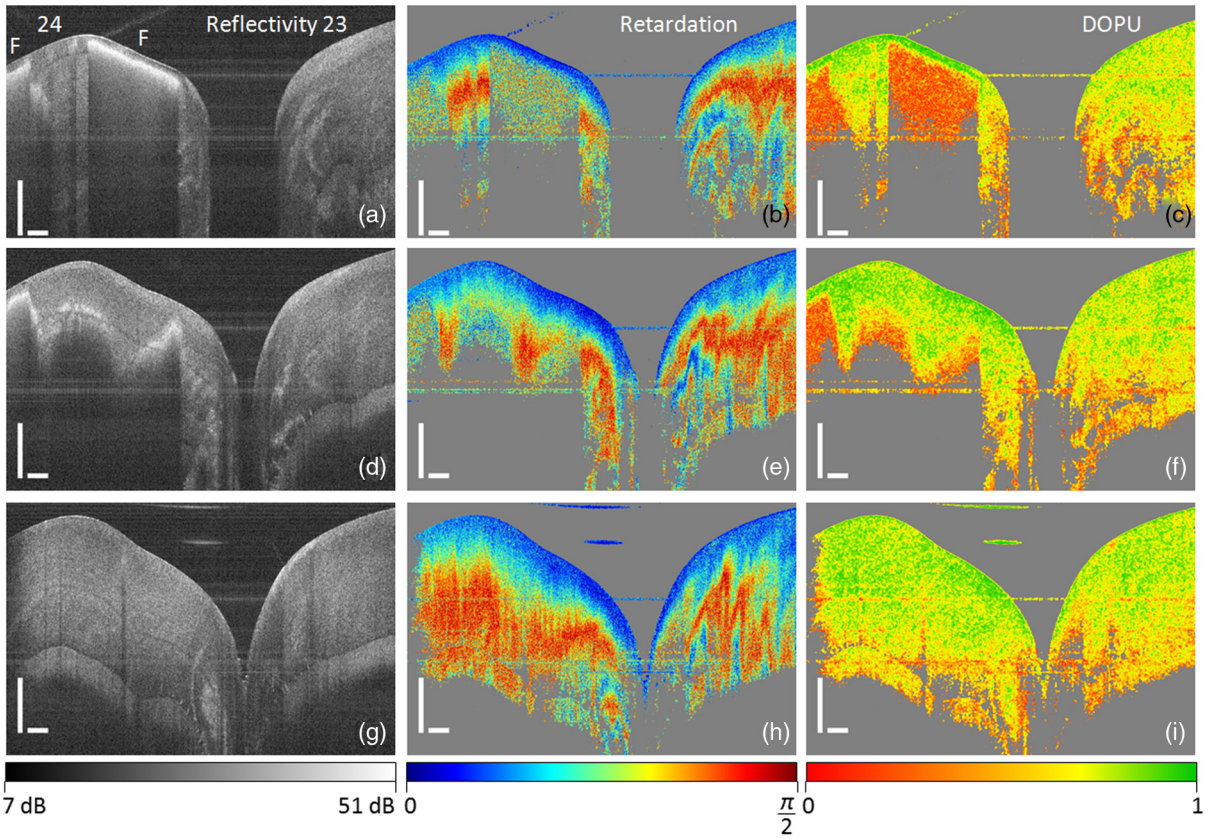

Fig. 6 Selected B-scans of the detected volume scan of the buccal surface of tooth 24 of volunteer A showing cross sections of (a–c) near-surface and (d–f) deep mineralization defect as well as of (g–i) the inconspicuous neighboring region. The approximate location of the B-scans is related to the bright blue dashed line in Fig. 3(b). Scale bars correspond to 500 μm. (Copolarized, crosspolarized, and optic axis orientation images in the appendix Figs. 15 and 16).

[cp. Fig. 3(c)], is detected at the transition to the gingiva. A polarization effect can be measured from the deeper region of the exposed dentin [$\delta(z) \sim \pi/2$ in Fig. 7(b)], which shows increased noise as validated by the DOPU cross section in Fig. 7(c). A higher retardation is also measured at the border area close to the gingiva [cross sign in Figs. 7(a) and 7(b)]. Selecting representative B-scans with enamel, imperfect mineralization can be identified within the enamel [asterisk in Figs. 7(d)–7(f)] but also a strong ablation of dentin [plus sign in Figs. 7(d)–7(f)]. Going further toward the lower cervical third, enamel is affected by mineralization irregularities at three regions [asterisk, hashtag, and circle in Figs. 7(g)–7(i)]. While the contrast in the reflectivity image is low, the DOPU visualization shows increased contrast for depolarization within and underneath the defect. Interestingly, the mineralization defect presented in Fig. 7 could clinically be seen only when a dental microscope was used. Regarding the gingiva, the imaging depth is partly reduced possibly due to the increased keratinization caused by traumatic tooth brushing.

3.3 *PS OCT of the Human Oral Mucosa In Vivo*

For evaluating the contrast advantage of PS OCT for *in vivo* imaging of oral soft tissue, three different regions of the anterior oral cavity are chosen with respect to the three main types of oral mucosa. First, the cervical region of tooth 21 of volunteer A is imaged with focus on the transition to the gingiva as an example for masticatory oral mucosa. Representative PS OCT image series are shown in Fig. 8 showing the increasing amount of gingiva relative to the cervical area of tooth 21. There, PS OCT provides an additional contrast likely caused by the gingival collagen fibers ensuring the attachment of the junctional epithelium to the tooth. With regard to the retardation and optic axis orientation shown in Figs. 8(b), 8(f), 8(j) and 8(c), 8(g), 8(k), different regions with strong birefringent behavior [asterisk in Figs. 8(a)–8(c) and 8(e)–8(g)] become apparent probably caused by fiber bundles bracing the gingiva against the tooth and being accessible by OCT in this region, e.g., dentogingival and intercircular fiber bundles. Also remarkable is the birefringent contrast in deeper regions within the gingiva [cross sign in Figs. 8(e)–8(g) and 8(i)–8(k)]. Since the optic axis orientation is strongly changing in this zone and not describable by a gradual increasing retardation due to cumulative measurement, the contrast in $\delta(z)$ and $\theta(z)$ is suggested to be caused by deep-lying fiber bundles, e.g., alveologingival fibers. Moreover, the closed gingiva above tooth 21 shows an increased polarization contrast [plus sign in Figs. 8(i)–8(k)].

Second, the inner side of the lower lip of volunteer A as representative lining oral mucosa is investigated by PS OCT. By means of the reflectivity images in Figs. 9(a) and 9(d), the low scattering epithelial layer (EP) above the highly scattering lamina propria (LP) are clearly differentiable. Apparently, few capillaries and labial glands (LG), belonging to the minor salivary glands, are identifiable as well. The asterisks in Figs. 9(a)

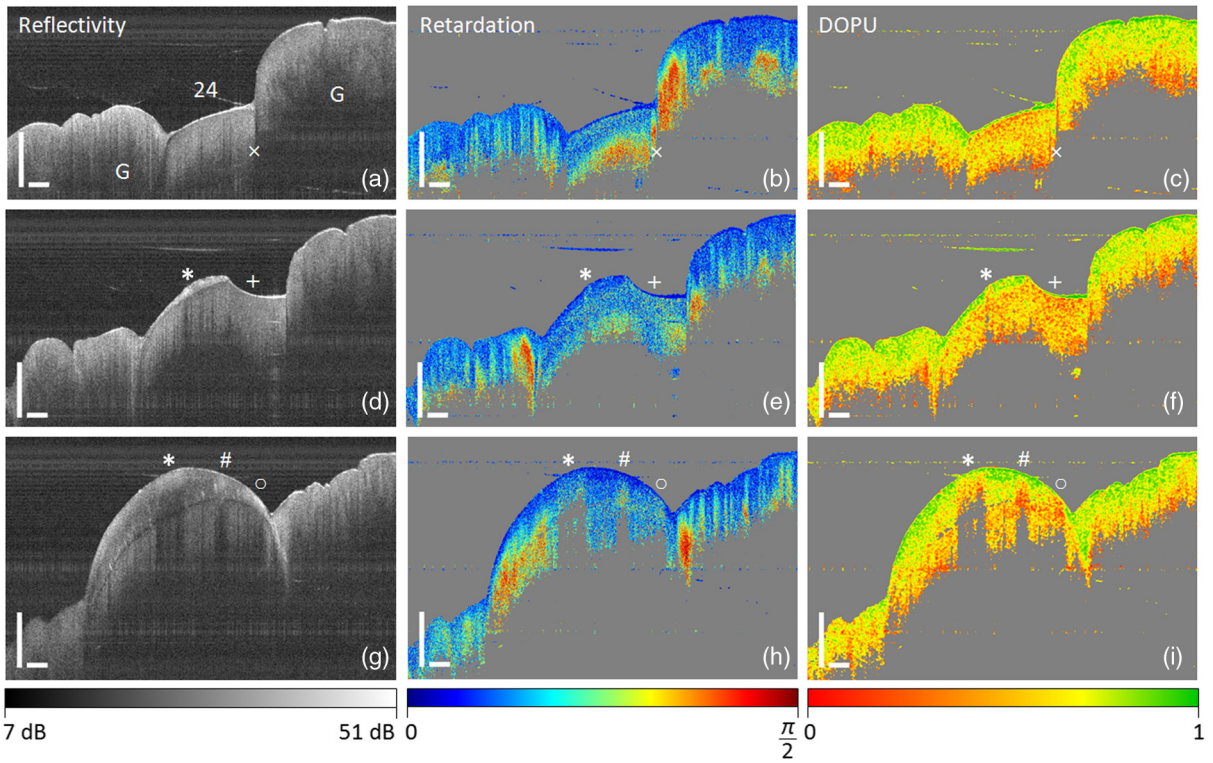

Fig. 7 Cervical area of tooth 24 of proband B showing (a–c) exposed dentin, (d–f) beginning enamel and partly ablated dentin as well as (g–i) enamel with early mineralization defect. The approximate location of the B-scans is related to the violet dashed line in Fig. 3(c). Cross sign: polarization change at the border area of the dentin close to the gingiva (G). Asterisk, hashtag, and circle: mineralization irregularities within the enamel. Plus sign: ablation region of the exposed dentin. Scale bars correspond to 500 μm. (Copolarized, crosspolarized, and optic axis orientation images in the appendix Figs. 17 and 18).

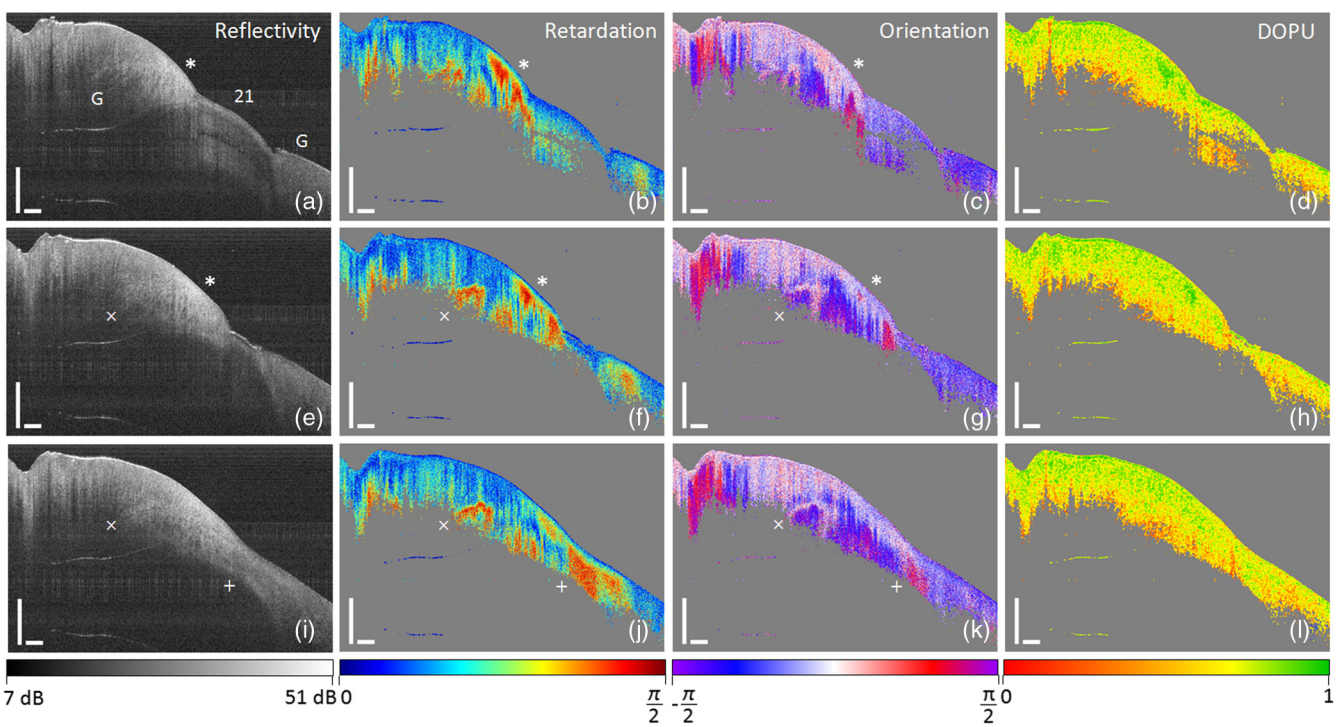

Fig. 8 Transition of tooth to gingiva (G) by means of the cervical region of tooth 21 of volunteer A. Regions with enhanced polarization contrast are suggested to be caused by, e.g., dentogingival and intercircular collagen fiber bundles (asterisk), alveologingival fibers (cross sign), and intergingival fibers (plus sign). The approximate location of the B-scans is related to the dark blue dashed line in Fig. 3(a). Scale bars correspond to 500 μm. (Co- and crosspolarized images in the appendix Fig. 19).

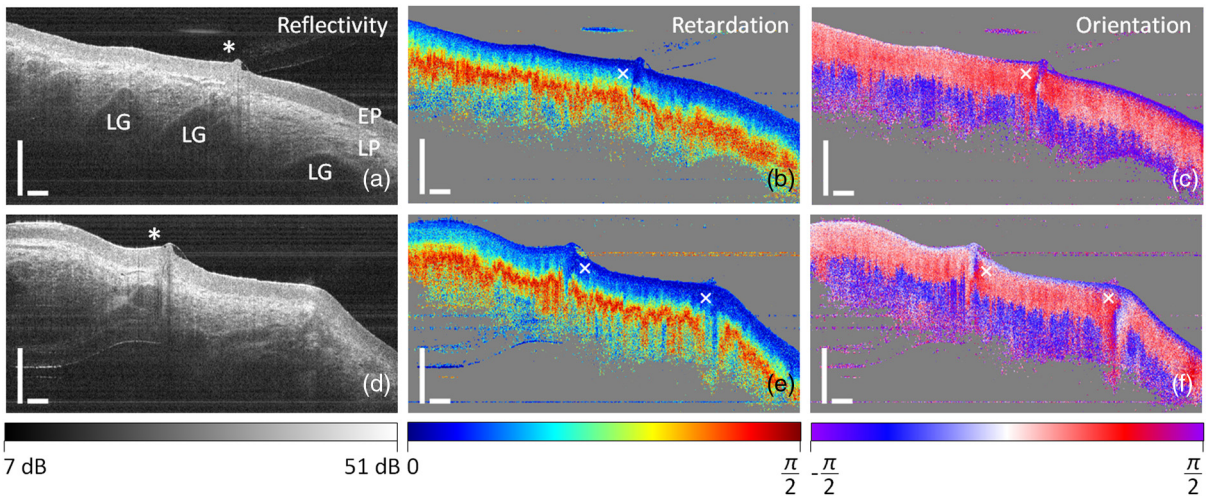

Fig. 9 Inner side of the lower lip of volunteer A representing exemplarily the lining mucosa detected by PS OCT to present the (a, d) reflectivity, (b, e) retardation, and (c, f) optic axis orientation. Asterisk: orifices of the labial salivary glands. EP, epithelium; LP, lamina propria; LG, labial gland. Cross sign: glandular openings are birefringent for which reason the optic axis orientation is lateral continuously changing with constant retardation. Scale bars correspond to 500 μm. (Copolarized, crosspolarized and DOPU images in the appendix Fig. 20).

and 9(d) mark gland duct orifices upon the mucous membrane showing a small reflex of the saliva at each orifice. Regarding the polarization contrast by means of retardation and optic axis orientation, a strong birefringence is detectable within the LP for the entire image width probably caused by the collagen fiber content. In addition, the excretory ducts are influencing the course of the collagen fiber bundles for which reason the retardation and optic axis orientation in the LP is different from

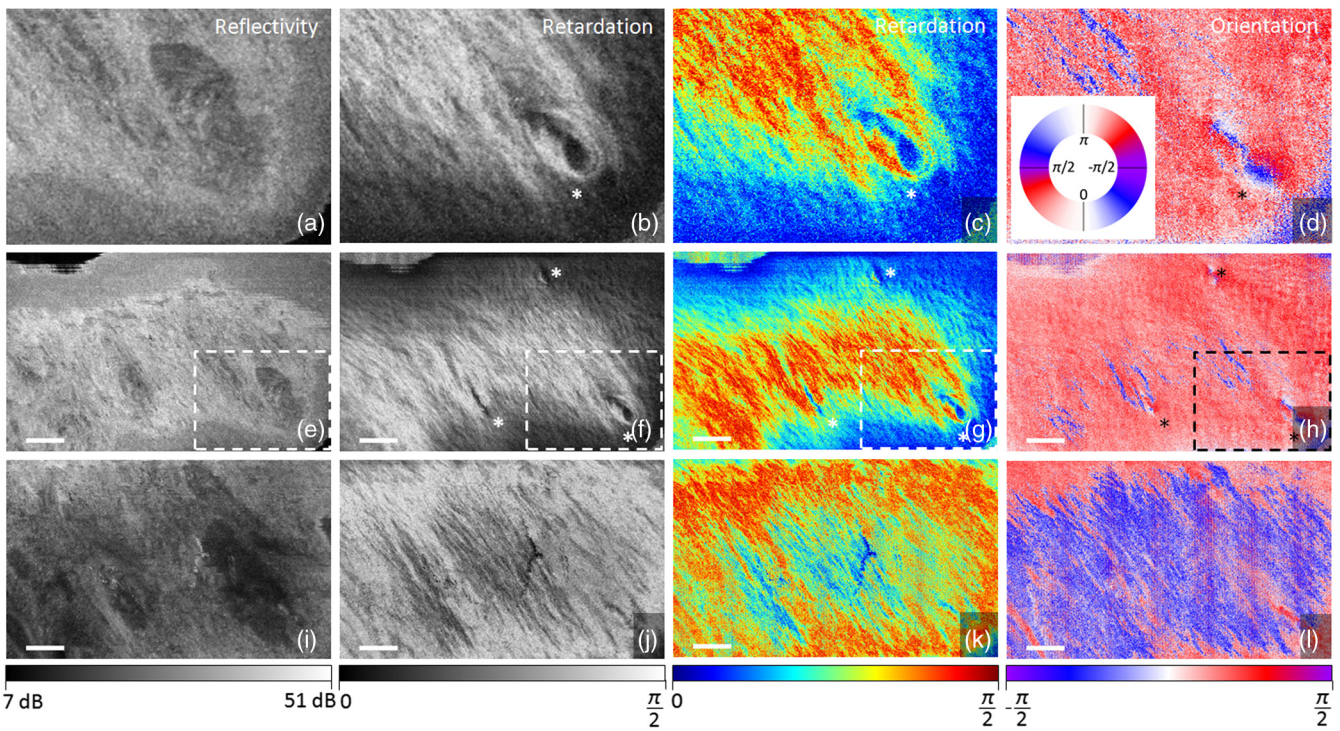

Fig. 10 *En face* images (single slices) of the labial oral mucosa of the inner side of the lower lip of volunteer A in a depth of (a–h) 380 and (i–l) 680 μm below the surface. There, (a–d) correspond to the enlarged view of the (e–h) lower right image part of the image series. Representative B-scans of the data set are shown in Fig. 9. Crosspolarization, retardation, and optic axis orientation images provide a significant contrast of the collagen fibers within the LP. Moreover, the circularly arranged fiber bundles arround the gland duct orifices can also be imaged with high contrast by the measured retardation and optic axis orientation [asterisks in (c, g) and (d, h)]. Scale bars correspond to 1 mm. (Copolarized, crosspolarized, and DOPU images in the appendix Fig. 21).

the surrounding tissue. Moreover, the glandular openings are surrounded by thin layers of connective tissue forming circular sheaths, which in turn are birefringent. There, the variable optic axis orientation of the birefringent fibers of the duct wall results in a measured lateral continuously running axis orientation with constant retardation [cross sign in Figs. 9(b), 9(c) and 9(e), 9(f)]. Furthermore, the rapid change of the measured optic axis orientation from $\theta(z) = \pi/3$ (red) to $\theta(z) = -\pi/3$ (blue) occurs for the cumulatively measured retardation of $\delta(z) = \pi/2$ and can be explained by means of Fig. 2(b).

En face images of the same data set (cp. Fig. 9) of the labial oral mucosa are generated and selected in different depths (about 380 and 680 μm beneath the surface) within the LP and shown in Fig. 10 [Figs. 10(a)–10(d) correspond to the enlarged view of Figs. 10(e)–10(h)]. The reflectivity images [Figs. 10(a), 10(e), and 10(i)] display the scattering structures of the connective tissue regardless of the birefringence properties. The polarization contrast of the almost linearly arranged birefringent collagen fibers becomes apparent by the retardation in grayscale [Figs. 10(b), 10(f), and 10(j)] and in color [Figs. 10(c), 10(g), and 10(k)] as well as the optic axis orientation [Figs. 10(d), (h), and 10(l)]. As shown in Figs. 10(b), 10(f), 10(j) and 10(c), 10(g), 10(k), the *en face* view of the retardation provides a strong contrast for the birefringent fiber structures within the LP. The gland duct orifices are clearly visible by their surrounding fiber structure and its birefringent behavior [asterisks in Figs. 10(b), 10(c) and 10(f), 10(g)]. Since the collagen fibers are circular surrounding the glandular ducts, the measured optic axis orientation is circularly changing at the corresponding regions [asterisks in Figs. 10(d) and 10(h)]. The circular color scale in Fig. 10(d) represents the fast axis orientation. The contrast difference between the measured retardation and optic axis orientation in Figs. 10(g), 10(h) and 10(k), 10(l) can be explained by means of the gradients of the color bars in the simulation in Fig. 2. While the measured retardation already provides a strong contrast for the cumulatively measured sample retardation smaller than $\pi/2$, the measured optic axis orientation changes abruptly at $\delta(z) = \pi/2$.

Third, the dorsal surface of the anterior outer third of the tongue body with distinctive specialized oral mucosa, containing mainly filiform papillae and occasionally distributed fungiform papillae, is imaged by PS OCT in volunteer A. Cross sectional reflectivity images in Figs. 11(a), 11(d), and 11(g) show the specialized mucosa of the anterior dorsal surface with two types of lingual papillae. Fungiform papillae [asterisk in Figs. 11(a) and 11(g)] are characterized by a thin nonkeratinized covering epithelium and a core of connective tissue, which both can be identified in Figs. 11(a) and 11(g). In contrast, filiform papillae [cross sign in Fig. 11(a)] are covered by a thick keratinized epithelium for which reason the imaging depth is decreased and therewith the papilla core and underlying structures are not detectable. Nevertheless, oral mucosa between the papillae permits a high imaging depth through the EP up to the LP. Considering the retardation and optic axis orientation images, a high polarization contrast in the regions between the papillae [plus signs in Figs. 11(b), 11(e), 11(h) and 11(c), 11(f), 11(i)] as well as in the deep reticular layer of the LP becomes apparent [hashtag in Figs. 11(b), 11(e), 11(h) and 11(c), 11(f), 11(i)]. For the transition regions, it is assumed that oriented collagen fiber bundles surrounding partly the

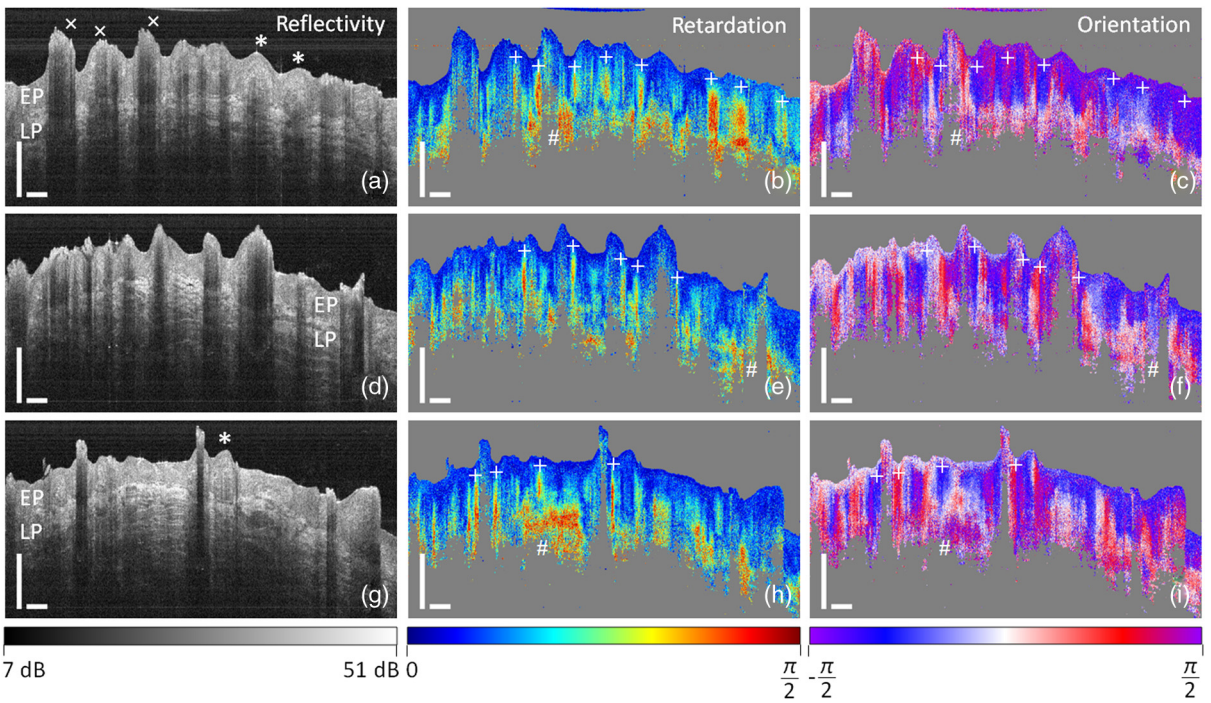

Fig. 11 Cross sectional images of the dorsal surface of the anterior outer third of the tongue body of volunteer A. Asterisk: Fungiform papillae with thin stratified squamous epithelium and connective tissue forming the papilla core. Cross sign: Filiform papillae with cornified tips resulting in high backscattering and strongly decreased imaging depth. Hashtag: Birefringent behavior of collagen fibers within the reticular layer of the LP cause a change in retardation. Plus sign: Polarization contrast probably due to outer collagen fibers of the connective tissue core of the papilla, EP, epithelium; LP lamina propria. Scale bars correspond to 500 μm. (Copolarized, crosspolarized, and DOPU images in the appendix Fig. 22.)

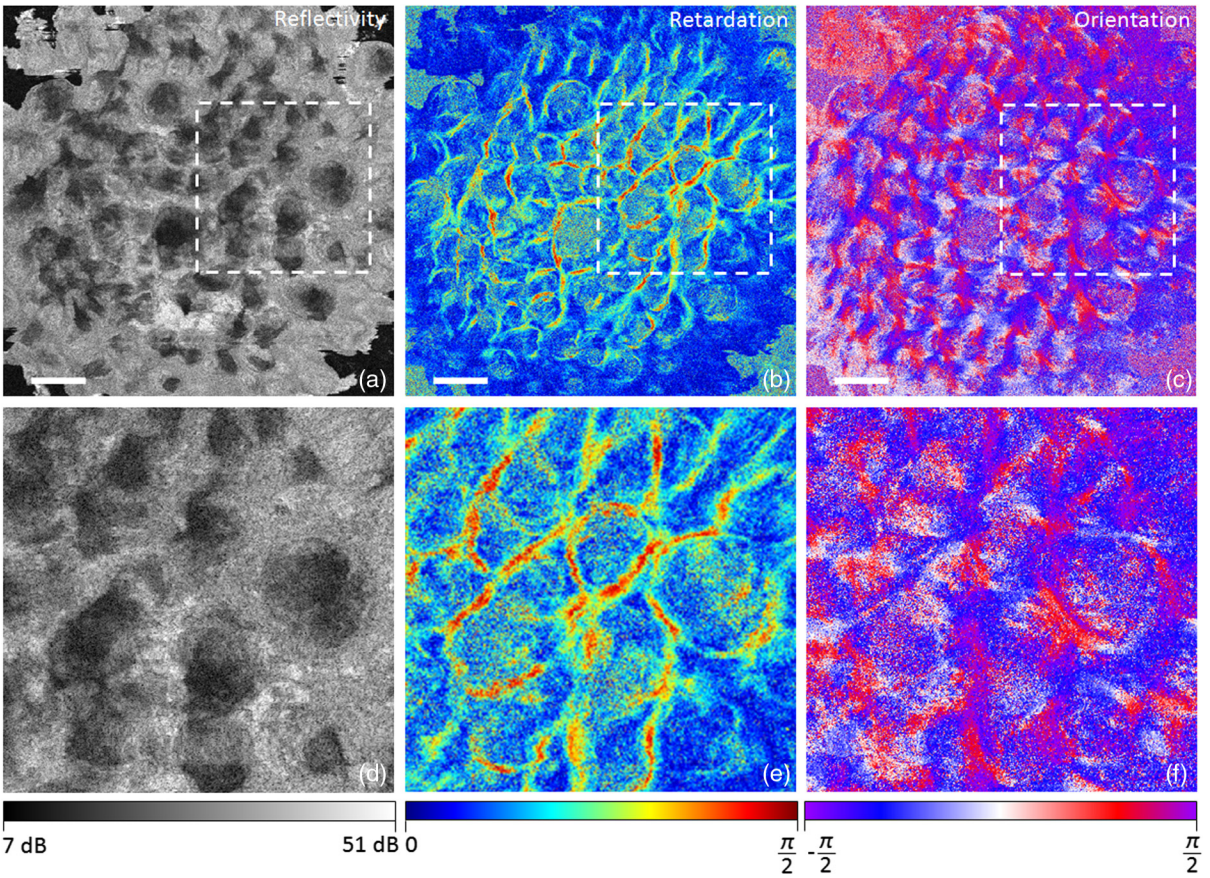

Fig. 12 *En face* images (single slices) showing the reflectivity, retardation, and optic axis orientation information in (a–c) a depth of 520 μm with (d–f) corresponding zoom view of the lingual mucosa of the dorsum of the tongue of volunteer A. Representative B-scans of the data set are shown in Fig. 11. Scale bars correspond to 1 mm. (Copolarized, crosspolarized, and DOPU images in the appendix Fig. 23.)

papilla core[49] cause the strong polarization contrast. Regarding the retardation within the core of the few fungiform papillae, no birefringent behavior is measured due to the randomly oriented collagen fibers of the connective tissue core.

Additionally, an *en face* projection of the determined reflectivity, retardation, and optic axis orientation in a specific depth of 520 μm is chosen and presented together with an enlarged view in Figs. 12(a)–12(c) and 12(d)–12(f). A contrast enhancement by means of the retardation and optic axis orientation becomes visible for the collagen fibers of the connective tissue in the transition parts between papillae.

4 Discussion and Summary

In this study, PS OCT with single circular input state in combination with the evaluation of reflectivity, retardation, optic axis orientation, and DOPU was used for cross sectional and *en face* imaging of hard and soft tissues in the anterior oral cavity. To the best of our knowledge, the value of this research is the visualization of retardation, optic axis orientation, and DOPU as polarization parameters in PS OCT, already established in ophthalmology, dermatology, and cardiology,[9,16] for the reliable interpretation of biological tissue with increased tissue-specific contrast in the human oral cavity *in vivo*.

Regarding the experimental results of oral hard tissues, circular polarized light incidence is advantageous in comparison to linear polarized incident light[19,20,33–39] since the fast or slow birefringent axis could coincide with the linear polarization undesirably resulting in the measurement of a strongly reduced or even no birefringence.[40] The additional information of retardation, optic axis orientation, and/or DOPU of the proposed method enables the precise local mapping of alterations to the surrounding inconspicuous birefringent tooth structures, which is highly recommended in future dental studies. In comparison to the reflectivity images, special characteristics within and underneath composite restorations are detectable making phase-sensitive PS OCT attractive for follow up monitoring of composite restorations and dental fillings. Furthermore and especially in comparison to the sole analysis of the images of the co- and crosspolarization channels,[34] peripheral regions of demineralization are more reliably determined by the combination of reflectivity and DOPU images, which should potentially be useful for routine monitoring in dentistry but also for basic research. Regarding the cervical region of teeth, the proposed imaging standard with PS OCT enables the imaging of the birefringent content of the gingiva, the structural characteristic of exposed birefringent dentin in the case of gingival recession as well as the validation of changes in mineralization of vulnerable enamel at exposed tooth necks. Moreover, the visualization of retardation, optic axis orientation, and DOPU in combination with the reflectivity imaging should be worthwhile to consider in *ex vivo* fundamental research and prospective clinical *in vivo* follow-up monitoring.

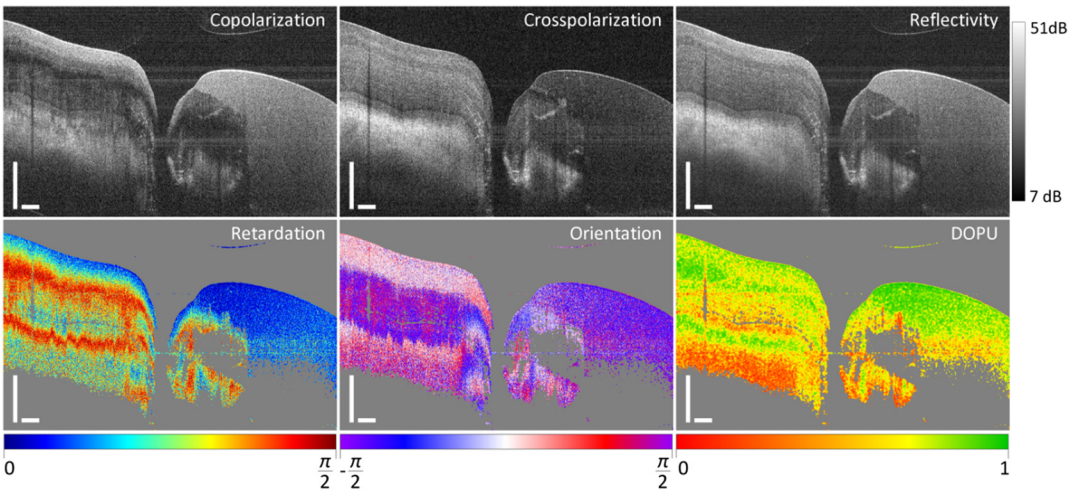

Fig. 13 (Appendix) In addition and complementary to Figs. 5(a)–5(c), copolarization, crosspolarization, reflectivity, retardation, optic axis orientation, and DOPU of the composite restoration at the proximal region of tooth 11 in comparison to the inconspicuous tooth 21 of volunteer A. Scale bars correspond to 500 μm.

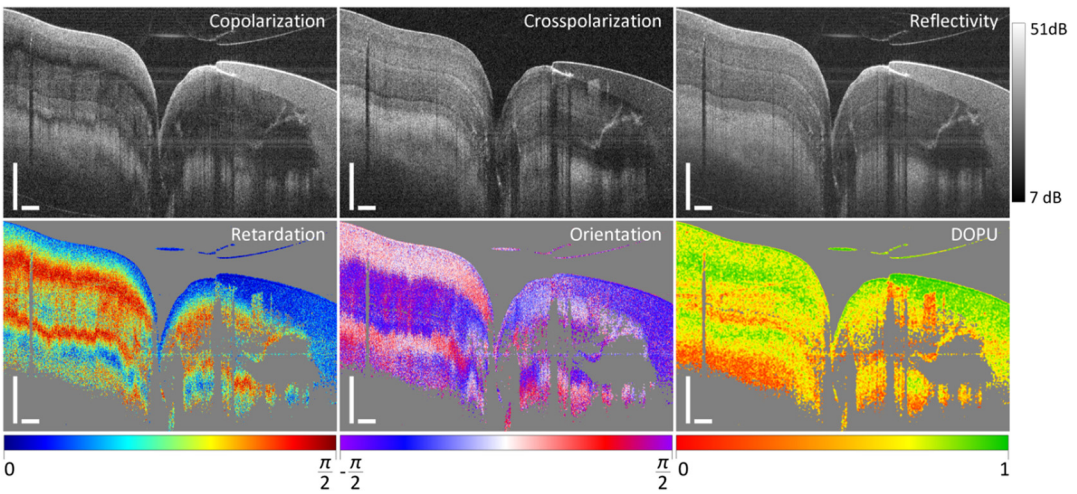

Fig. 14 (Appendix) In addition and complementary to Figs. 5(g)–5(i), copolarization, crosspolarization, reflectivity, retardation, optic axis orientation, and DOPU of the composite restoration at the proximal region of tooth 11 in comparison to the inconspicuous tooth 21 of volunteer A. Scale bars correspond to 500 μm.

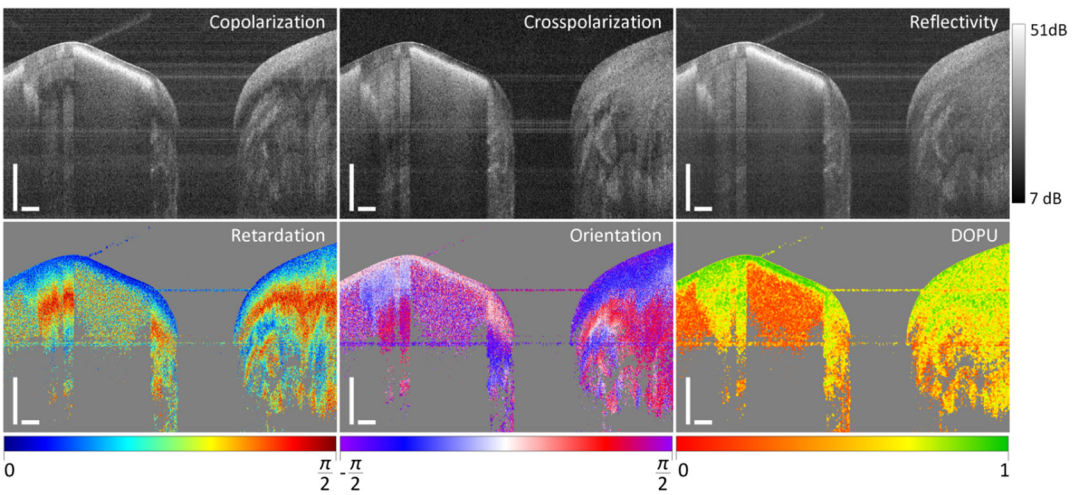

Fig. 15 (Appendix) In addition and complementary to Figs. 6(a)–6(c), copolarization, crosspolarization, reflectivity, retardation, optic axis orientation, and DOPU of the near-surface mineralization defect at the buccal surface of tooth 24 of volunteer A. Scale bars correspond to 500 μm.

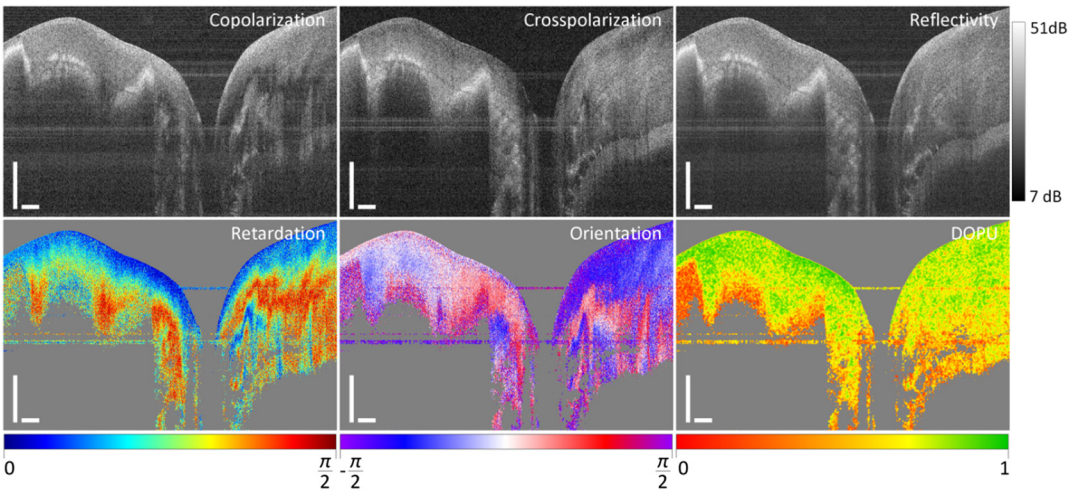

Fig. 16 (Appendix) In addition and complementary to Figs. 6(d)–6(f), copolarization, crosspolarization, reflectivity, retardation, optic axis orientation, and DOPU of the deep mineralization defect at the buccal surface of tooth 24 of volunteer A. Scale bars correspond to 500 μm.

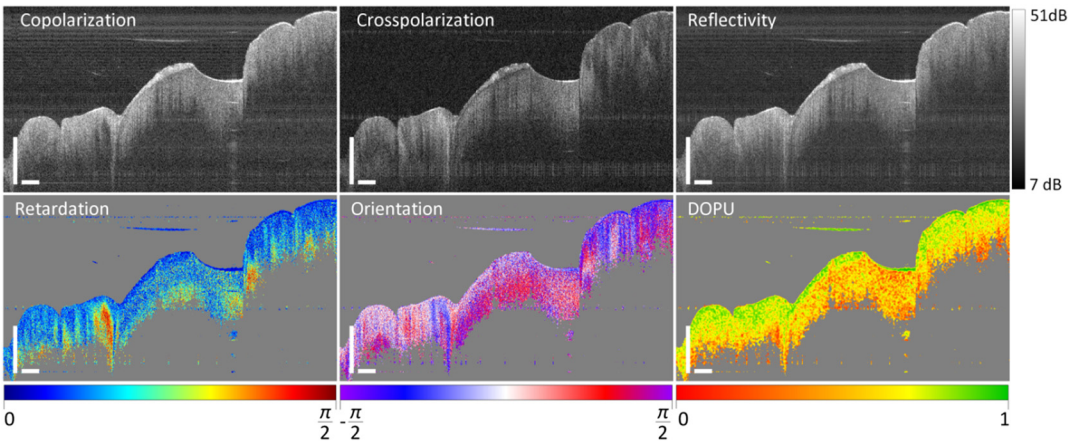

Fig. 17 (Appendix) In addition and complementary to Figs. 7(d)–7(f), copolarization, crosspolarization, reflectivity, retardation, optic axis orientation, and DOPU of the cervical area of tooth 24 of proband B showing beginning enamel and partly ablated dentin. Scale bars correspond to 500 μm.

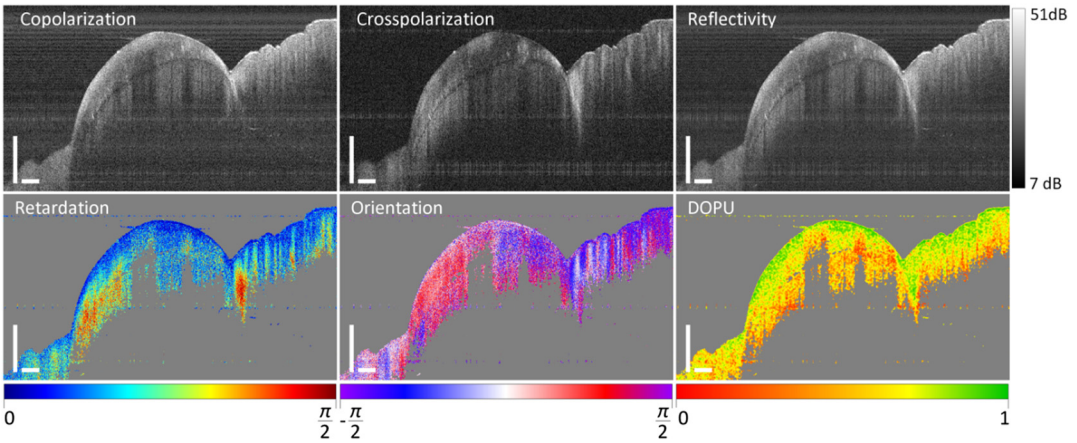

Fig. 18 (Appendix) In addition and complementary to Figs. 7(g)–7(i), copolarization, crosspolarization, reflectivity, retardation, optic axis orientation, and DOPU of the cervical area of tooth 24 of proband B showing enamel with early mineralization defect. Scale bars correspond to 500 μm.

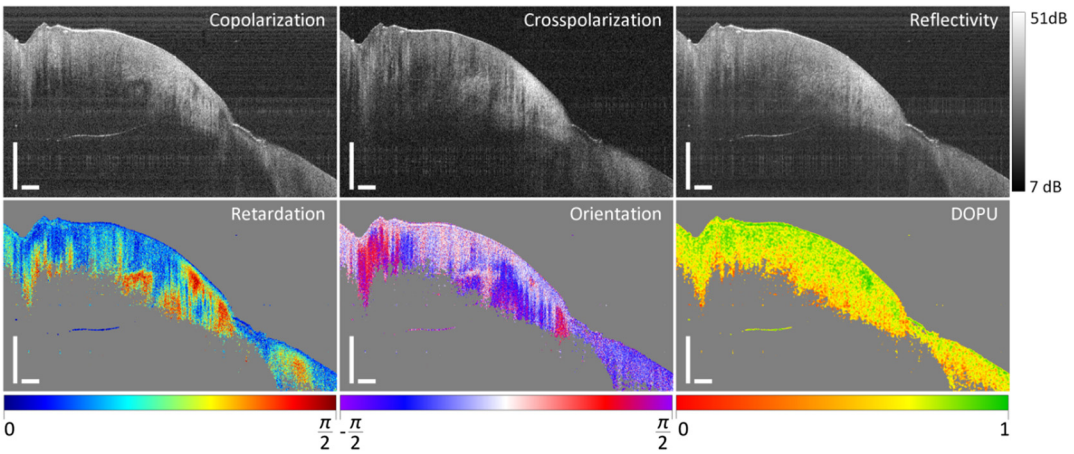

Fig. 19 (Appendix) In addition and complementary to Figs. 8(e)–8(h), copolarization, crosspolarization, reflectivity, retardation, optic axis orientation, and DOPU of the transition of tooth to gingiva by means of the cervical region of tooth 21 of volunteer A. Scale bars correspond to 500 μm.

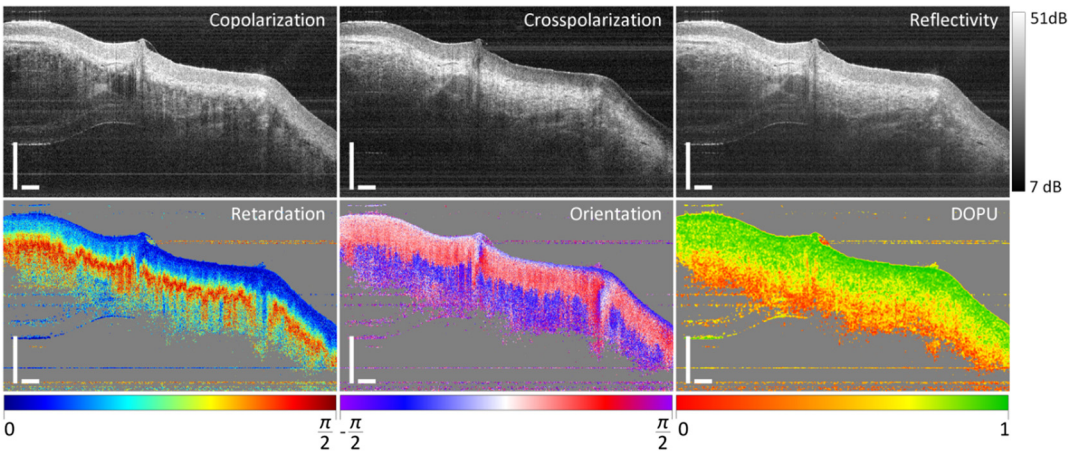

Fig. 20 (Appendix) In addition and complementary to Figs. 9(d)–9(f), copolarization, crosspolarization, reflectivity, retardation, optic axis orientation, and DOPU of the inner side of the lower lip of volunteer A. Scale bars correspond to 500 μm.

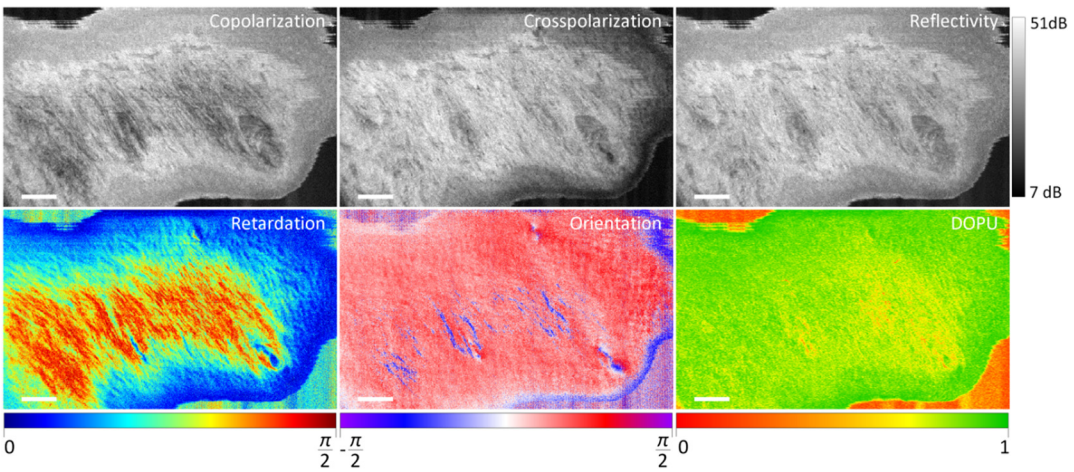

Fig. 21 (Appendix) In addition and complementary to Figs. 10(e)–10(h), copolarization, crosspolarization, reflectivity, retardation, optic axis orientation, and DOPU of the e*n face* images of the labial oral mucosa of the inner side of the lower lip of volunteer A in a depth of 380 μm below the surface. Scale bars correspond to 1 mm.

Since most of the alterations of oral soft tissue are visually detected in dentistry, the application of PS OCT in this study was expanded to the oral mucosa. Also in this field of application, the proposed PS OCT offers a tissue-specific contrast for the linear aligned collagen fiber bundles in the reticular layer of the lamina propria in the case of lining oral mucosa but also for specific tissue regions with embedded collagen fibers in the case of the specialized oral mucosa, e.g., the dorsum of the tongue. With this background and the future extension to the entire oral cavity, the precise detection of structural changes within the birefringent region of the lamina propria is conceivable.[32,52] Moreover, PS OCT probably has the potential to detect the borders of altered oral tissue more reliably due to the enhanced tissue contrast compared to neighboring unchanged tissues.

In summary, the utilization of the phase-sensitive detection of the backscattering signal in two orthogonal polarization channels and the determination of the parameters reflectivity, retardation, optic axis orientation, and depolarization is state-of-the-art in various biomedical applications of PS OCT and enables a detailed physical interpretation of the investigated biological tissue such as oral hard and soft tissues as presented in this research. The results of the pilot study show the potential of PS OCT, with single circular polarization input state and adapted data processing, for the *in vivo* imaging of oral tissues on the example of the anterior oral cavity. Because of the simultaneous information of morphology by the reflectivity and polarization properties by retardation, optic axis orientation and DOPU, PS OCT with phase-sensitive detection is highly

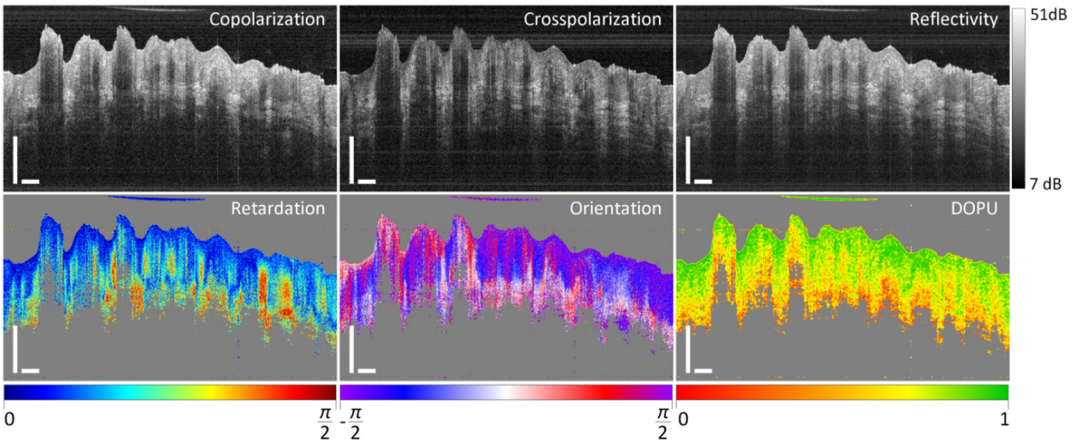

Fig. 22 (Appendix) In addition and complementary to Figs. 11(a)–11(c), copolarization, crosspolarization, reflectivity, retardation, optic axis orientation, and DOPU of the dorsal surface of the anterior outer third of the tongue body of volunteer A. Scale bars correspond to 500 μm.

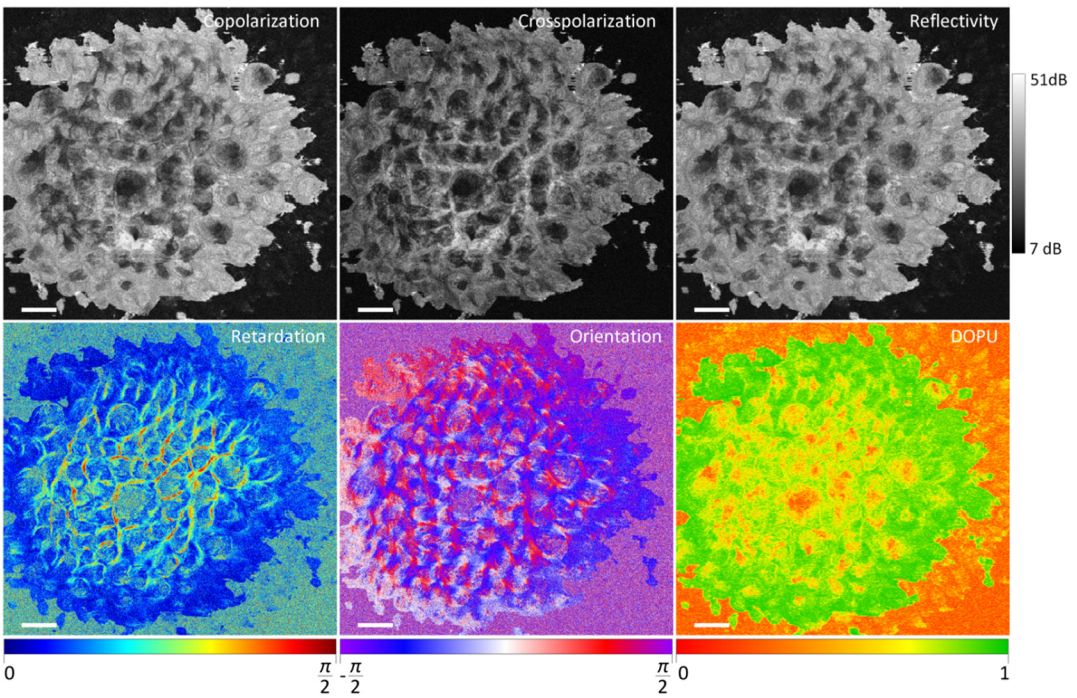

Fig. 23 (Appendix) In addition and complementary to Figs. 12(a)–12(c), copolarization, crosspolarization, reflectivity, retardation, optic axis orientation, and DOPU of the *en face* images of the lingual mucosa of the dorsum of the tongue of volunteer A in a depth of 520 μm. Scale bars correspond to 1 mm.

recommended for depth-resolved clinical imaging of oral hard and soft tissues in the future.

Appendix

For the completeness and transparency of the presented experimental data, images of the co- and crosspolarization channel as well as reflectivity, retardation, optic axis orientation and DOPU are prepared in addition to Figs. 5–12.

Disclosures

The PS OCT imaging of the human oral cavity by the homebuilt system was reviewed and approved by the developers employed at the Technische Universität Dresden, and the informed consent was obtained from all subjects before imaging. Both human subjects included in this pilot study are developers of the applied OCT system and main author of the paper who decided to be volunteers on their own responsibility. Accordingly, the responsible local ethics committee waved the need for an approval. The study followed the tenets of the Declaration of Helsinki and was conducted in compliance with Health Insurance Portability and Accountability Act. Furthermore, the authors declare that there are no conflicts of interest related to this article.

Acknowledgments

This project was supported by the European Union/European Social Fund (ESF) and the Free State of Saxony within the ESF junior research group "Optical Technologies in Medicine" (project number 100270108). The author Jonas Golde is supported by the European Union/European Social Fund (ESF) and the Free State of Saxony within a doctoral scholarship (project number 100284305).

References

1. D. Huang et al., "Optical coherence tomography," *Science* **254**, 1178–1181 (1991).
2. W. Drexler and J. G. Fujimoto, *Optical Coherence Tomography Technology and Applications*, Springer, Berlin, Heidelberg, Germany, New York (2008).
3. S. Marschall et al., "Optical coherence tomography-current technology and applications in clinical and biomedical research," *Anal. Bioanal. Chem.* **400**(9), 2699–2720 (2011).
4. J. Walther et al., "Optical coherence tomography in biomedical research," *Anal. Bioanal. Chem.* **400**(9), 2721–2743 (2011).
5. N. Gladkova et al., "Cross-polarization optical coherence tomography for early bladder-cancer detection: statistical study," *J. Biophotonics* **4**(7–8), 519–532 (2011).
6. E. Kiseleva et al., "Differential diagnosis of human bladder mucosa pathologies in vivo with cross-polarization optical coherence tomography," *Biomed. Opt. Express* **6**(4), 1464–1476 (2015).
7. M. R. Hee et al., "Polarization-sensitive low-coherence reflectometer for birefringence characterization and ranging," *J. Opt. Soc. Am. B* **9**(6), 903–908 (1992).
8. J. F. de Boer et al., "Two-dimensional birefringence imaging in biological tissue by polarization-sensitive optical coherence tomography," *Opt. Lett.* **22**(12), 934–936 (1997).
9. B. Baumann, "Polarization sensitive optical coherence tomography: a review of technology and applications," *Appl. Sci.* **7**(5), 474 (2017).
10. M. J. Everett et al., "Birefringence characterization of biological tissue by use of optical coherence tomography," *Opt. Lett.* **23**(3), 228–230 (1998).
11. C. K. Hitzenberger et al., "Measurement and imaging of birefringence and optic axis orientation by phase resolved polarization sensitive optical coherence tomography," *Opt. Express* **9**(13), 780–790 (2001).
12. E. Götzinger, M. Pircher, and C. K. Hitzenberger, "High speed spectral domain polarization sensitive optical coherence tomography of human retina," *Opt. Express* **13**(25), 10217–10229 (2005).
13. E. Götzinger et al., "Retinal pigment epithelium segmentation by polarization sensitive optical coherence tomography," *Opt. Express* **16** (21), 16410–16422 (2008).
14. B. Baumann et al., "Segmentation and quantification of retinal lesions in age-related macular degeneration using polarization-sensitive optical coherence tomography," *J. Biomed. Opt.*, **15**(6), 061704 (2010).
15. J. F. de Boer and T. E. Milner, "Review of polarization sensitive optical coherence tomography and Stokes vector determination," *J. Biomed. Opt.* **7**(3), 359–371 (2002).
16. J. F. de Boer, C. K. Hitzenberger, and Y. Yasuno, "Polarization sensitive optical coherence tomography: a review," *Biomed. Opt. Express* **8**(3), 1838–1873 (2017).
17. W. Drexler and J. G. Fujimoto, "State-of-the-art retinal optical coherence tomography," *Prog. Retinal Eye Res.* **27**(1), 45–88 (2008).
18. M. Pircher, C. K. Hitzenberger, and U. Schmidt-Erfurth, "Polarization sensitive optical coherence tomography in the human eye," *Prog. Retinal Eye Res.* **30**(6), 431–451 (2011).
19. D. Fried et al., "Imaging caries lesions and lesion progression with polarization sensitive optical coherence tomography," *J. Biomed. Opt.* **7**(4), 618–627 (2002).
20. T. Louie et al., "Clinical assessment of early tooth demineralization using polarization sensitive optical coherence tomography," *Lasers Surg. Med.* **42**(10), 898–905 (2010).
21. S. K. Nadkarni, "Optical measurement of arterial mechanical properties: from atherosclerotic plaque initiation to rupture," *J. Biomed. Opt.* **18**(12), 121507 (2013).
22. S. K. Nadkarni et al., "Measurement of collagen and smooth muscle cell content in atherosclerotic plaques using polarization-sensitive optical coherence tomography," *J. Am. Coll. Cardiol.* **49**(13), 1474–1481 (2007).
23. S. Sakai et al., "In vivo evaluation of human skin anisotropy by polarization-sensitive optical coherence tomography," *Biomed. Opt. Express* **2**(9), 2623–2631 (2011).
24. P. Gong et al., "Imaging of skin birefringence for human scar assessment using polarization-sensitive optical coherence tomography aided by vascular masking," *J. Biomed. Opt.* **19**(12), 126014 (2014).
25. M. Bonesi et al., "High-speed polarization sensitive optical coherence tomography scan engine based on Fourier domain mode locked laser," *Biomed. Opt. Express* **3**(11), 2987–3000 (2012).
26. X.-J. Wang et al., "Characterization of dentin and enamel by use of optical coherence tomography," *Appl. Opt.* **38**(10), 2092–2096 (1999).
27. A. Baumgartner et al., "Polarization-sensitive optical coherence tomography of dental structures," *Caries Res.* **34**(1), 59–69 (2000).
28. Y.-S. Hsieh et al., "Dental optical coherence tomography," *Sensors* **13**(7), 8928–8949 (2013).
29. K. H. Kim et al., "Polarization-sensitive optical frequency domain imaging based on unpolarized light," *Opt. Express* **19**(2), 552–561 (2011).
30. Y. Yoon et al., "In vivo wide-field reflectance/fluorescence imaging and polarization-sensitive optical coherence tomography of human oral cavity with a forward-viewing probe," *Biomed. Opt. Express* **6**(2), 524–534 (2015).
31. A. M. D. Lee et al., "Wide-field in vivo oral OCT imaging," *Biomed. Opt. Express* **6**(7), 2664–2674 (2015).
32. P. Sharma et al., "Human ex-vivo oral tissue imaging using spectral domain polarization sensitive optical coherence tomography," *Lasers Med. Sci.* **32**(1), 143–150 (2017).
33. R. Jones, M. Staninec, and D. Fried, "Imaging artificial caries under composite sealants and restorations," *J. Biomed. Opt.* **9**(6), 1297–1304 (2004).
34. P. Ngaotheppitak, C. L. Darling, and D. Fried, "Measurement of the severity of natural smooth surface (interproximal) caries lesions with polarization sensitive optical coherence tomography," *Lasers Surg. Med.* **37**(1), 78–88 (2005).
35. R. S. Jones et al., "Imaging artificial caries on the occlusal surfaces with polarization-sensitive optical coherence tomography," *Caries Res.* **40**(2), 81–89 (2006).
36. R. Jones et al., "Remineralization of in vitro dental caries assessed with polarization-sensitive optical coherence tomography," *J. Biomed. Opt.* **11**(1), 014016 (2006).

37. S. K. Manesh, C. L. Darling, and D. Fried, "Polarization-sensitive optical coherence tomography for the nondestructive assessment of the remineralization of dentin," *J. Biomed. Opt.* **14**(4), 044002 (2009).
38. H. Tom et al., "Near-infrared imaging of demineralization under sealants," *J. Biomed. Opt.* **19**(7), 077003 (2014).
39. P. Lenton et al., "Clinical cross-polarization optical coherence tomography assessment of subsurface enamel below dental resin composite restorations," *J. Med. Imaging* **1**(1), 016001 (2014).
40. Y. Chen, L. Otis, and Q. Zhu, "Study tissue polarization with polarization-sensitive OCT by linearly and circularly polarized probing light," *Proc. SPIE* **5690**, 446-452 (2005).
41. B. W. Colston, Jr. et al., "Imaging of the oral cavity using optical coherence tomography," *Monogr. Oral. Sci.* **17**, 32-55 (2000).
42. Y. Chen et al., "Characterization of dentin, enamel, and carious lesions by a polarization-sensitive optical coherence tomography system," *Appl. Optics* **44**(11), 2041–2048 (2005).
43. S. M. Douglas, D. Fried, and C. L. Darling, "Imaging natural occlusal caries lesions with optical coherence tomography," *Proc. SPIE* **7549**, 75490N (2010).
44. X. Ni and R. R. Alfano, "Time-resolved backscattering of circularly and linearly polarized light in turbid media," *Opt. Lett.* **29**(23), 2773–2775 (2004).
45. Y. Chen, L. Otis, and Q. Zhu, "Polarization memory effect in optical coherence tomography and dental imaging application," *J. Biomed. Opt.* **16**(8), 086005 (2011).
46. J. Schindelin et al., "Fiji: an open-source platform for biological-image analysis," *Nat. Methods* **9**(7), 676–682, (2012).
47. L. Raue et al., "New insights in prism orientation within human enamel," *Arch. Oral Biol.* **57**(3), 271–276 (2012).
48. A. C. Deymier-Black et al., "Synchrotron x-ray diffraction study of load partitioning during elastic deformation of bovine dentin," *Acta Biomater.* **6**(6), 2172–2180 (2010).
49. S. Emura, T. Okumura, and H. Chen, "Morphology of the lingual papillae and their connective tissue cores in the cape hyrax," *Okajimas Folia Anat. Jpn.* **85**(1), 29–34 (2008).
50. A. R. TenCate, *Oral Histology: Development, Structure and Function*, 4th ed., Mosby, St. Martins, London (1998).
51. Z. Meng et al., "Measurement of the refractive index of human teeth by optical coherence tomography," *J. Biomed. Opt.* **14**(3), 034010 (2009).
52. N. Gladkova et al., "Evaluation of oral mucoa collagen condition with cross-polarization optical coherence tomography," *J. Biophotonics* **6**(4), 321–329 (2013).

Julia Walther is a senior researcher at the Technische Universität Dresden. She received her diploma in physics technology and biomedical engineering from the University of Applied Sciences Mittweida in 2006 and her PhD in medical physics and biomedical optics from the Technische Universität Dresden in 2010. Her current research interests include the advancement of optical coherence tomography (OCT) for different applications in dentistry and otolaryngology as well as the analysis and extension of diverse theoretical models for Doppler OCT (DOCT).

Jonas Golde is a PhD student at the Technische Universität Dresden. He received his MSc degree in physics from the Technische Universität Dresden in 2016 with a thesis on polarization-sensitive optical coherence tomography (PS OCT). Since then, he has been focused on the development and application of PS OCT systems in the fields of dentistry and otolaryngology. His research interests include the combination of PS-OCT with complementary optical technologies, such as multiphoton microscopy and hyperspectral imaging.

Lars Kirsten is a senior researcher at the research group Clinical Sensoring and Monitoring of Prof. Dr. Edmund Koch at the Technische Universität Dresden. He joined the research group in 2009 and received his diploma in physics in 2010 and his PhD (Dr. rer. nat.) in 2015. Since 2016, he has been the leader of the junior research group Optical Technologies in Medicine. His current research interests include OCT, especially the further development of polarization-sensitive OCT, DOCT, endoscopic OCT, and their applications in otolaryngology, dentistry, and biomedical basic research.

Florian Tetschke received his MSc degree in biomedical engineering from the University of Applied Sciences Jena in 2013. He contributed to research projects at the Biomagnetic Center of the University Hospital in Jena, at the Polytechnical University of Catalonia, and the Institute of Biomedical Engineering at the Technische Universität Dresden. Currently, he is a research associate at the junior research group, "Optical Technologies in Medicine" at the Technische Universität Dresden. His research interest focuses on the development and application of optical technologies, such as hyperspectral imaging, OCT, and Raman spectroscopy.

Franz Hempel received his BSc degree in physics from the Technische Universität Dresden in 2017. He wrote his thesis on PS OCT in the work group Clinical Sensoring and Monitoring at the Medical Faculty of the Technische Universität Dresden. His research interests include the application of PS OCT in biomedical imaging.

Tobias Rosenauer is a dentist and a research associate of the University Clinic Carl Gustav Carus in Dresden. He graduated in 2016 and has since then worked for the Department of Operative Dentistry, TU Dresden. He is currently writing his doctoral thesis and his present research concerns cariological aspects as well as optical imaging.

Christian Hannig is head of the Department of Operative Dentistry, TU Dresden. Furthermore, he is the dean for dental education. He has been a dentist since 2000 and has worked at Göttingen and Freiburg University before coming to Dresden. His main field of research is bioadhesion in the oral cavity. He is author of more than 100 international and national journal papers. His research has been funded several times by the German Research Foundation.

Edmund Koch received his diploma and PhD degrees in physics from the University of Marburg. He worked as a senior researcher at Drägerwerke AG, Lübeck, and thereafter he became professor for laser and optics at Lübeck University of Applied Sciences. He is currently head of the work group Clinical Sensoring and Monitoring at the Faculty of Medicine at the TU Dresden. His main research interests are OCT and spectroscopic imaging.